UNIVERSITY OF CALIFORNIA
RIVERSIDE

Multi-Scale Optical Coherence Tomography Imaging

A Dissertation submitted in partial satisfaction
of the requirements for the degree of

Doctor of Philosophy

in

Bioengineering

by

Michael Christopher Oliveira

August 2014

Dissertation Committee:
Dr. B. Hyle Park, Chairperson
Dr. Dimitrios Morikis
Dr. William Grover

The Dissertation of Michael Christopher Oliveira is approved:

_____

_____

_____

Committee Chairperson

University of California, Riverside

ACKNOWLEDGEMENTS

I want to express my utmost gratitude to my thesis advisor Professor Hyle Park for his unwavering support and mentorship during the past five years. He was never too busy to take the time to answer questions, review written work, discuss research related problems and solutions and entertain crazy ideas that I came up with. His commitment to the success of his students is second to none and I'm proud to have been a student of his.

I want to thank all the members of my qualifying and dissertation defense committees for their support and guidance over the past five years (Professor Dimitrios Morikis, Professor William Grover, Professor Victor Rodgers, Professor Andre Obenaus, Professor Huinan Liu, and Professor Peter Hickmott).

I also want to thank the past and present members of the Neuroscience and Optical Imaging Research group at the University of California, Riverside. The trailblazing work of Yan Wang, Md. Shahidul Islam and Christian Oh to establish the lab was instrumental to my success. I especially want to thank Md. Rezuanul Haque for being a wonderful colleague and friend during our graduate school careers together. Lastly, I want to thank Koji Hirota, Jonathon Ma, Carissa Rodriguez and Melissa Eberle for making the lab a fun and productive work environment during my time at the University of California, Riverside.

In addition, I was fortunate enough to participate in the National Science Foundation Integrative Graduate Education, Research and Training program in Video Bioinformatics program during my final three years at the University of California,

Riverside. I am extremely grateful for the financial support and interdisciplinary education and training that will serve me well throughout my career.

Finally, I want to acknowledge the love and support from my parents. I am eternally grateful for everything they have done to get me to this point in my life.

I thank the Optical Society of America (OSA) for permission to include portions of Chapter 2 that was originally published in Optics Express. I thank the International Society for Optics and Photonics (SPIE) for permission to include portions of Chapter 3 that was originally published in the Journal of Biomedical Optics. Financial support was provided by awards from the National Institutes of Health (R00EB007241), National Science Foundation Integrative Graduate Education, Research and Training program in Video Bioinformatics (NSF IGERT: Video Bioinformatics Grant DGE 0903667) and the SPIE Optics and Photonics Education Scholarship.

ABSTRACT OF THE DISSERTATION

Multi-Scale Optical Coherence Tomography Imaging

by

Michael Christopher Oliveira

Doctor of Philosophy, Graduate Program in Bioengineering
University of California, Riverside, August 2014
Professor B. Hyle Park, Chairperson

An optical modality capable of quantitative, label-free, high-speed and high-resolution imaging across spatiotemporal scales coupled with sophisticated software for image reconstruction and quantitative analyses would be of great utility to scientists and engineers in the medical and life sciences fields. Currently, a combination of optical imaging techniques and software packages are needed to address the list of capabilities described previously. Optical coherence tomography is an optical imaging technique based on low coherence interferometry capable of measuring light backscattered from the sample at micrometer-level resolutions over millimeter-level penetration depths in biological tissue. Phase-sensitive extensions of OCT enable the functional assessment of biological tissue samples as well as the structural examination of samples down to the single-cell level. This dissertation describes the development and application of high-speed real-time multi-functional spectral-domain OCT (MF-SD-OCT) for structural and functional examination of biological samples across spatiotemporal scales. A discussion

of the development of a GPU-accelerated high-speed MF-SD-OCT imaging system accompanied by demonstrations of the performance enhancements due to the GPU are presented initially. Next, the development of MF-SD-OCT-based quantitative methods for the structural and functional assessment and characterization and classification of biological tissue samples is discussed. The utility of these methods is demonstrated through structural, functional and optical characterization and classification of peripheral nerve and muscle tissue. The dissertation concludes with a discussion of the improvements made to spectral-domain optical coherence phase microscopy (SD-OCPM) to enable dynamic live cell imaging and the application of dynamic live cell SD-OCPM for morphological visualization of cheek epithelial cells and examination of functionally stimulated morphological changes in neurons. The work described in this dissertation demonstrates the versatility of OCT imaging technology to perform quantitative, label-free, high-speed and high-resolution imaging across spatiotemporal scales, enabling the examination of native dynamic tissue and cellular physiology.

TABLE OF CONTENTS

LIST OF FIGURES

LIST OF TABLES

Introduction

Since its inception in the early 1990's, OCT has emerged as an optical imaging modality with applications spanning many fields in biology and medicine [1]. OCT has become well known as the optical analog to ultrasound imaging due to the similarity in the operating principles of the two technologies. Using near-infrared light as the source instead of acoustic sound waves, OCT can achieve light penetration depths of 2 mm in highly scattering media such as biological tissue with micrometer-level spatial resolution. Cross-sectional images can be built up by measuring the magnitude and echo-time delay of light scattered from a sample compared to light reflected back from a reference. Detection electronics are not fast enough to precisely measure the echo-time delay so detection is typically done using a Michelson interferometer and serves as the basis of OCT imaging for spectral-domain OCT systems. Phase-sensitive extensions of OCT enable the functional assessment of biological tissue samples as well as the structural examination of samples down to the single-cell level. Polarization-sensitive OCT profiles the polarization properties of tissue and can be used to assess tissue health and physiology. Doppler OCT examines the Doppler shift induced in the reflected light waves by moving scatterers and can be used to spatially resolve and measure fluid flow within tissue. Phase-resolved Doppler OCT (PRD-OCT) examines phase changes due to displacement over a small period of time to reconstruct images of fluid flow. Optical coherence phase microscopy enables the resolution of nanometer-level optical path length mismatches in the interferometer that are used to reconstruct quantitative phase images of

single cell samples. The combination of OCT and its extensions result in a powerful tool for examining important problems across the medical and life sciences fields.

The purpose of this dissertation is to discuss the development of multi-scale visualization and analytical methods for biological tissue and cellular samples. Effective multi-scale visualization requires the development of a graphics processing unit (GPU)-accelerated multi-functional spectral-domain OCT (MF-SD-OCT) system capable of on-line processing and image reconstruction. Accurate multi-scale analytical methods require the development and application of MF-SD-OCT-based methods for structural and optical characterization and classification of biological tissue and cellular samples. The first chapter provides background into MF-SD-OCT imaging. It describes the operating principles behind low-coherence interferometry, SD-OCT and phase-sensitive extensions of SD-OCT (polarization-sensitive and Phase-resolved Doppler OCT) and lays the mathematical foundation of these techniques necessary for understanding the latter chapters of the dissertation.

The second chapter focuses on the development of a MF-SD-OCT system in which the on-line MF-SD-OCT data processing has been off-loaded to a GPU for real-time, high-speed MF-SD-OCT imaging. The chapter begins with an introduction to serial and parallel computing paradigms and the CUDA programming platform used to develop the GPU-accelerated MF-SD-OCT data processing algorithms. The unique contributions to this chapter are the development of GPU-accelerated 2D and 3D MF-SD-OCT data processing workflows using CUDA for high-speed 2D and 3D data visualization. Demonstrations of the speedup achieved over CPU-based MF-SD-OCT data processing

are shown by benchmarking and comparing the performance GPU-based processing and CPU-based processing and by high-speed 2D and 3D MF-SD-OCT imaging of a variety of biological samples. The chapter concludes with discussions of the results of the speedup obtained and the utility of a real-time MF-SD-OCT imaging system as well as some suggestions for future development.

The third chapter focuses on the application of MF-SD-OCT imaging technology for quantitative assessment of biological tissue samples. The chapter begins with an introduction to basic concepts in biophotonics and light-tissue interactions necessary to understand how the quantitative assessment of biological tissue samples was performed. The unique contributions in this chapter are the development of quantitative methods to structurally characterize peripheral nerve tissue and measure the optical properties of peripheral nerve and muscle tissues for health assessment and classification purposes. The chapter concludes with a discussion of the results of the quantitative assessments methods and their importance in the assessment of nerve health and injury.

The final chapter of the dissertation focuses on the development of a quantitative phase microscopy extension of SD-OCT for visualization and analysis of biological samples at the cellular level. The chapter begins with an introduction to the theory behind spectral-domain optical coherence phase microscopy (SD-OCPM) and the requirements for performing dynamic live cell SD-OCPM imaging. The unique contributions in this chapter are in the improvement of traditional SD-OCPM imaging for performing dynamic live cell imaging and quantitative assessment of dynamic cellular physiology without the need for a reference surface near the sample. Demonstrations of the improved

technology are done by structural SD-OCPM imaging of a cheek epithelial cell and time-lapse SD-OCPM imaging and quantitative morphological assessment of neurons before and after the addition of the neurotransmitter glutamate. The chapter concludes with discussions of the benefits of performing quantitative label-free imaging of cellular samples, important considerations for performing dynamic live cell SD-OCPM imaging and the results of the SD-OCPM imaging demonstrations.

Chapter 1: Multi-functional spectral-domain optical coherence tomography theory

This chapter describes the theoretical and mathematical foundation of multi-functional spectral domain optical coherence tomography. The chapter is organized into three main sections: an introduction to low-coherence interferometry (Section 1.1) and spectral domain optical coherence tomography (Section 1.2), an introduction to polarization-sensitive optical coherence tomography (Section 1.3) and the Jones matrix- (Section 1.3.1) and Stokes vector-based (Section 1.3.2) methods and an introduction to Doppler optical coherence tomography (Section 1.4) and the bi-directional and phase variance-based methods.

Section 1.1: Low-coherence interferometry

Low-coherence interferometry is the technology that underlies OCT imaging. The Michelson interferometer is the most widely used interferometer when constructing OCT systems. Following the conventions of Izatt and Choma [2], consider an interferometer illuminated by a polychromatic plane wave whose complex electric field can be expressed as:

$$E_{src} = s\left(k,\omega\right)e^{\left(i\left[kz-\omega t\right]\right)} \tag{1.1}$$

where k is the wavenumber ($2\pi/\lambda$), ω is the angular frequency ($2\pi\nu$), z is the optical path length along the propagation direction, t is time, $s(k,\omega)$ is the amplitude of the electric field and $e^{(i[kz-\omega t])}$ is the complex phase as a function of spatial and temporal frequencies. The wave is incident on an achromatic beam splitter with a 0.5 splitting ratio

and is split between a reference arm and sample arm. The electric fields at the reference and sample arms can be described by:

$$E_R = \frac{E_{src}}{\sqrt{2}} r_R e^{i2kz_R} \tag{1.2}$$

$$E_S = \frac{E_{src}}{\sqrt{2}} \left(r_s(z_S) \otimes e^{i2kz_S} \right) \tag{1.3}$$

where $\otimes$ is the convolution operator, r_R is the reference electric field reflectivity, z_R and z_S are the reference and sample optical path lengths respectively and $r_s(z_S)$ describes the depth-dependent reflectivity in the sample arm. This reflectivity can be modeled as a series of N discrete reflectors with reflectivity r_{s_n} and optical path length z_{s_n} and is of the form $r_s(z_S) = \sum_{n=1}^{N} r_{s_n} \delta(z_S - z_{s_n})$. In biology however, the reflectivity of the sample is best described by a continuous distribution of reflectors due to the continuous distribution of biological material with differing refractive indices. Light reflected back from the reference and sample arms interfere at the beam splitter and are detected by a square-law detector in the detection arm. The photocurrent generated can be described as follows:

$$I_D(k,\omega) = \frac{\rho}{2} \left\langle E_R + E_S \right\rangle^2 \tag{1.4}$$

where ρ is the responsivity of the detector, E_R and E_S are the reference and sample electric fields respectively and the angular brackets denote integration over the detector response time. Setting the zero position for the optical path lengths at the beam splitter, substituting equations (1.2) and (1.3) into (1.4) and expanding for the detector current results in:

$$I_D(k) = \frac{\rho}{4}\left[S(k)\left(R_R + R_{S_1} + R_{S_2} + \ldots\right)\right] + \frac{\rho}{4}\left[S(k)\sum_{n=1}^{N}\sqrt{R_R R_{S_n}}\left(e^{i2k\left(z_R - z_{S_n}\right)} + e^{-i2k\left(z_R - z_{S_n}\right)}\right)\right] + \frac{\rho}{4}\left[S(k)\sum_{n\neq m=1}^{N}\sqrt{R_{S_n} R_{S_m}}\left(e^{i2k\left(z_{S_n} - z_{S_m}\right)} + e^{-i2k\left(z_{S_n} - z_{S_m}\right)}\right)\right] \quad (1.5)$$

where $S(k) = \langle |s(k,\omega)|^2 \rangle$ is the power spectral density of the source. The above equation can be further simplified using Euler's rule and results in the spectral interferogram:

$$I_D(k) = \frac{\rho}{4}\left[S(k)\left(R_R + R_{S_1} + R_{S_2} + \ldots\right)\right] + \frac{\rho}{2}\left[S(k)\sum_{n=1}^{N}\sqrt{R_R R_{S_n}}\left(\cos 2k\left(z_R - z_{S_n}\right)\right)\right] + \frac{\rho}{4}\left[S(k)\sum_{n\neq m=1}^{N}\sqrt{R_{S_n} R_{S_m}}\left(\cos 2k\left(z_{S_n} - z_{S_m}\right)\right)\right] \quad (1.6)$$

where the first term describes the DC terms, the second term describes the cross-correlation between the reference reflector and each sample arm reflector and the final term describes the auto-correlation between reflectors within the sample arm. It can be seen from the above equation that specific optical path length mismatches between the reference reflector and sample reflectors results in specific output frequencies at the detector. In the case of a sample containing multiple reflectors, the spectral interferogram is modulated with multiple cosinusoids, each with a frequency that corresponds to the optical path length mismatch between a given sample reflector and the reference reflector.

Section 1.2: Spectral-domain optical coherence tomography (SD-OCT)

As mentioned previously, detection of the echo-time delay between light reflected back from a sample arm with respect to light reflected back from a reference arm is done

via interferometry. OCT systems are comprised of the same source, reference, sample and detections arms commonly found in interferometry setups. The first report on OCT was published in *Science* by Huang et al. in 1991 [1]. The technology has rapidly developed over the past 20 years accelerated by advancements in the telecommunications, optics and computing industries. Early OCT systems were time-domain systems in which the reference arm of the interferometer was scanned and the interference detected as a function of time [3,4,5,6]. Second generation systems were Fourier-domain systems in which the reference arm remained stationary and the interference was detected as a function of wavenumber using a spectrometer (spectral-domain) [7,8] or a point detector (swept-source/optical frequency domain imaging) [9]. These second generation systems boast superior sensitivity and imaging speeds due to the reduction of noise achieved by dispersing the detection of the interference over wavenumber space [10,11,12]. The detection of the spectral interference is processed with Fourier analysis to determine the depth-resolved reflectivity of the sample. An inverse Fourier transform of (1.6) results in the following equation:

$$\begin{aligned} i_D(z) = \frac{\rho}{8}\left[\gamma(z)\left(R_R + R_{S_1} + R_{S_2} + \ldots\right)\right] + \frac{\rho}{4}\left[\gamma(z) \otimes \sum_{n=1}^{N} \sqrt{R_R R_{S_n}} \left(\delta\left(z \pm 2\left(z_R - z_{S_n}\right)\right)\right)\right] \\ + \frac{\rho}{8}\left[\gamma(z) \otimes \sum_{n \neq m=1}^{N} \sqrt{R_{S_n} R_{S_m}} \left(\delta\left(z \pm 2\left(z_{S_n} - z_{S_m}\right)\right)\right)\right] \end{aligned} \tag{1.7}$$

where $\gamma(z)$ is the coherence function (the inverse Fourier transform of the source spectrum), $\delta\left(z \pm 2\left(z_R - z_{S_n}\right)\right)$ is the delta function describing the positions of sample reflectors interfering with the reference reflector and $\delta\left(z \pm 2\left(z_{S_n} - z_{S_m}\right)\right)$ is the delta

function describing the positions of sample reflectors interfering within the sample arm. Carrying out the convolution operations results in the final depth resolved reflectivity measurement, commonly called an "A-line" in OCT:

$$\begin{aligned} i_D(z) = & \frac{\rho}{8}\left[\gamma(z)\left(R_R + R_{S_1} + R_{S_2} + \ldots\right)\right] \\ & + \frac{\rho}{4}\left[\sum_{n=1}^{N}\sqrt{R_R R_{S_n}}\left(\gamma\left[+2\left(z_R - z_{S_n}\right)\right] + \gamma\left[-2\left(z_R - z_{S_n}\right)\right]\right)\right] \\ & + \frac{\rho}{8}\left[\sum_{n\neq m=1}^{N}\sqrt{R_{S_n} R_{S_m}}\left(\gamma\left[+2\left(z_{S_n} - z_{S_m}\right)\right] + \gamma\left[-2\left(z_{S_n} - z_{S_m}\right)\right]\right)\right] \end{aligned} \tag{1.8}$$

There are a number of important considerations described by the A-line equation for SD-OCT. The DC and auto-correlation terms create artifacts around the zero delay position that can be easily avoided. Additionally, due to the properties of the Fourier transform, a mirror image of the depth-resolved sample reflectivity exists on the opposite side of the zero delay position. This complex-conjugate artifact is typically removed by displaying only one of the images.

The spectral interferogram described by (1.6) contains all the information necessary to generate a complex-value A-line from which OCT, polarization-sensitive OCT (PS-OCT) and Phase-resolved Doppler OCT (PRD-OCT) information can be obtained. Interferograms are unevenly spaced in wavenumber and require remapping to evenly spaced wavenumbers to avoid the broadening of the axial point spread function (aPSF) that reduces the axial resolution of SD-OCT systems [13]. Because of the remapping processing, interpolation of the interferogram at the new evenly spaced wavenumbers is done prior to taking the inverse Fourier transform. The interpolation process can be improved by zero-padding the interferogram beforehand. Inverse Fourier

transform of the interpolated interferogram results in the complex-value A-lines (1.8) from which the magnitude and phase can be used to generate structural OCT images and functional PS-OCT and D-OCT images respectively. Acquisition of A-lines as a beam is raster scanned across a biological sample result in complex-value 2D (B-line) and 3D (C-line) data. OCT images can be formed by computing the intensity from all complex-value A-lines that comprise an image:

$$I_n(z_m) = H_n(z_m) \cdot \tilde{H}_n(z_m) \tag{1.9}$$

where H is the complex-value image comprised of n number of A-lines of length m determined by the size of the pixel array of the camera used in the spectrometer and ~ is the complex conjugate operator. For multi-camera SD-OCT systems (such as those used in PS-OCT), the intensity is the sum of the intensities detected in both cameras:

$$I_n(z_m) = H_n(z_m) \cdot \tilde{H}_n(z_m) + V_n(z_m) \cdot \tilde{V}_n(z_m) \tag{1.10}$$

where V represents the complex value image of the second camera with an identical size to H. Intensity values are typically displayed using a logarithmic gray scale. Depth-resolved intensity distributions are indicative of spatial variations of scattering of biological tissue. These spatial variations of scattering can be resolved to within 1-15 μm depending on the wavelength of the source used (axial resolution) and optics in the sample arm (lateral resolution).

For the purposes of this this dissertation, spatial resolution is defined as the minimum distance two objects can be separated by and still be seen as two separate objects. Axial resolution defines the ability of an imaging system to visualize two points separated in depth. The convolution operations in (1.7) blur the position of each reflector

in the cross-correlation and auto-correlation terms to the width of the coherence length of the light source and define the aPSF of the OCT system. The axial resolution of the OCT system is directly related to the coherence length of the light source used and can be described by the following relationship:

$$l_c = \frac{2ln(2)}{\pi}\frac{\lambda_0^2}{\Delta\lambda} \tag{1.11}$$

where λ_0 is the center wavelength of the light source and $\Delta\lambda$ is the spectral bandwidth of the source defined as the full-width half-maximum (FWHM) of the full wavelength spectrum. The inverse relationship between the coherence length and the spectral bandwidth informs us that axial resolution in OCT can be increased by using larger spectral bandwidth sources. Lateral resolution defines the ability of an imaging system to visualize two points separated in plane. In OCT, the optics used in the sampling arm dictate the lateral resolution of the system. Assuming the sampling arm optics are similar to confocal geometrical optics and a point reflector is placed at the focal plane of the system, the lateral resolution of an OCT system can be described the FWHM of the lateral PSF:

$$\delta x = 0.37\frac{\lambda_0}{NA} \tag{1.12}$$

where NA is the numerical aperture of the final lens of the OCT sampling arm.

Section 1.3: Polarization-sensitive optical coherence tomography (PS-OCT)

Polarization-sensitive OCT (PS-OCT) is a functional extension of OCT used to perform high-resolution mapping of tissue health and physiology [14,15,16,17,18]. PS-

OCT uses a polarized light source to obtain contrast specific to certain biological tissues that exhibit polarization-dependent phenomena (diattenuation or birefringence, discussed below). Two formalisms exist to mathematically describe these polarization-dependent light-tissue interactions and are used to extract quantitative measures of diattenuation and birefringence of biological samples: the Jones formalism [19] and Stokes formalism [20]. Polarization-dependent light-tissue interactions that alter the amplitude ratio or phase difference between orthogonal electric field components of light result from well-organized cylindrical structures that comprise biological tissues. Tissues with this type of microstructure offer additional contrast that can be visualized and measured using PS-OCT. PS-OCT has been widely used to visualize human skin [21,22], assess the extent of burn wounds [23,24,25] and examine the health of the eye [17].

Light is a transverse wave and its electric field can be completely described by the amplitudes, frequencies and phases of its horizontal and vertical components:

$$\vec{E} = a_{\parallel} e^{-i\delta_{\parallel}} \hat{e}_{\parallel} + a_{\perp} e^{-i\delta_{\perp}} \hat{e}_{\perp} \tag{1.13}$$

where $a_{||}$ and $a_{\perp}$ are the amplitudes of the horizontal and vertical components respectively, $\delta_{||}$ and $\delta_{\perp}$ are the phases of the horizontal and vertical electric field components respectively and $\hat{e}_{||}$ and $\hat{e}_{\perp}$ are the unit vectors along the horizontal and vertical directions. Generally speaking, a polarization state is considered to be elliptical and its exact state is defined by the amplitude ratio and phase difference between the electric field components. Linear polarization states occur for any amplitude ratio and $\Delta\delta = \delta_{||} - \delta_{\perp} = 0$ between components and circular polarization states occur for equal

amplitude ratios ($a_{||} = a_{\perp}$) and integer-multiples of the phase difference ($\Delta\delta = \frac{\pi}{2} + n\pi$) between components.

Materials that alter the polarization state of light are classified into two effects: diattenuation and birefringence. Diattenuation describes changes in the amplitude ratio and birefringence describes changes in the phase difference between the electric field components respectively. Diattenuating, or dichroic, materials are materials that attenuate light polarized parallel to its optic axis differently than light polarized perpendicular to its optic axis. Defining P_1 and P_2 as the amplitude ratios between incident and transmitted light for light waves polarized parallel and perpendicular to the optic axis of a diattenuating material (dichroic material), diattenuation can be expressed by the following ratio:

$$d = \frac{P_1^2 - P_2^2}{P_1^2 + P_2^2} \tag{1.14}$$

Values for diattenuation range from zero to one inclusive. Birefringent materials are materials that have a different refractive index depending on the polarization state of the light traveling through it. This induces a phase lag between the electric field components that are parallel and perpendicular to the optic axis the material. Defining η as the phase difference between the orthogonal electric field components, birefringence can be expressed by the following equation:

$$\Delta n = \frac{\eta\lambda}{2\pi x} \tag{1.15}$$

where λ is the wavelength of the light and x is the physical distance traveled by the light waves. Typical values of birefringence for biological tissue are on the order of ~0.001.

Birefringence is the dominant polarization-dependent effect in biological samples. Two main methods exist for the computation of birefringence in PS-OCT: the Jones matrix-based method [19] and simplified Stokes vector-based method [20].

Section 1.3.1: Jones matrix based method

The Jones matrix based method is a convenient formalism to use when working with purely polarized light. The electric field components described in (1.13) can be written as a complex 2-element vector known as a Jones vector:

$$E = E_{\parallel}\hat{e}_{\parallel} + E_{\perp}\hat{e}_{\perp} = \begin{bmatrix} E_{\parallel} \\ E_{\perp} \end{bmatrix} \tag{1.16}$$

These complex 2-element Jones vectors can be related to one another using 2x2 matrices known as Jones matrices. These matrices can be used to describe the polarization properties of any non-depolarizing material. A transmitted polarization state E' can be described by the effects on an incident polarization state E after traveling through material defined by a Jones matrix J:

$$E' = \begin{bmatrix} E_{\parallel}' \\ E_{\perp}' \end{bmatrix} = e^{i\psi} \begin{bmatrix} J_{11} & J_{12} \\ J_{21} & J_{22} \end{bmatrix} \begin{bmatrix} E_{\parallel} \\ E_{\perp} \end{bmatrix} = e^{i\psi} JE \tag{1.17}$$

where J represents the 2x2 Jones matrix of the non-depolarizing material, E is the incident Jones vector, E' is the transmitted Jones vector and ψ is an arbitrary phase. If the incident polarization state E travels through a series of n materials, each described by a unique Jones matrix J_n, the transmitted state E' is described by the combined effects of the Jones matrices J_n acting on the incident state E, i.e. $E' = e^{i\psi}(J_n \ldots J_2 J_1)E$.

Unique Jones matrices exist to describe dichroic and birefringent materials. Following the notation from Park [27], the Jones matrix for a dichroic material with attenuation ratios P_1 and P_2 and an optic axis orientation described by θ and ϕ can be described as follows:

$$J_d = \begin{bmatrix} P_1 \cos^2\theta + P_2 \sin^2\theta & (P_1 - P_2)\cos\theta \sin\theta e^{-i\phi} \\ (P_1 - P_2)\cos\theta \sin\theta e^{i\phi} & P_1 \sin^2\theta + P_2 \cos^2\theta \end{bmatrix} \tag{1.18}$$

The Jones matrix describing birefringent materials follows a similar form. For a given phase retardance η between orthogonal polarization states and an optic axis orientation and circularity described by Θ and Φ respectively, the Jones matrix for birefringence can be described by the following equation:

$$J_b = \begin{bmatrix} e^{i\eta/2}\cos^2\Theta + e^{-i\eta/2}\sin^2\Theta & \left(e^{i\eta/2} - e^{-i\eta/2}\right)\cos\Theta \sin\Theta e^{-i\Phi} \\ \left(e^{i\eta/2} - e^{-i\eta/2}\right)\cos\Theta \sin\Theta e^{i\Phi} & e^{i\eta/2}\sin^2\Theta + e^{-i\eta/2}\cos^2\Theta \end{bmatrix} \tag{1.19}$$

PS-OCT systems and the samples imaged by such systems can be described in terms of Jones vectors and matrices. Let J_{in} represent the Jones matrix that describes the optical path from the polarized light source to the surface of a sample, J_{out} represent the Jones matrix that describes the optical path from the sample surface to the detectors in a polarization-sensitive spectrometer and J_S represent the Jones matrix of the round-trip light propagation through the sample. The electric field reflected back from some depth within the sample detected by the spectrometer can be described as:

$$E' = e^{i\Delta\psi} J_{out} J_S J_{in} E \tag{1.20}$$

where E is the electric field emitted by the polarized light source. Assuming negligible diattenuation in the system and that J_S can be decomposed into a central diagonal matrix

containing the diattenuation and phase retardance of the sample and surrounding matrices defining the optic axis orientation of both polarization effects, the polarization parameters of the sample being imaged can be determined as follows:

$$\begin{bmatrix} P_1 e^{i\eta/2} & 0 \\ 0 & P_2 e^{-i\eta/2} \end{bmatrix} = e^{i\Delta\psi} \begin{bmatrix} \cos\Theta & \sin\Theta \\ -\sin\Theta & \cos\Theta \end{bmatrix} \begin{bmatrix} e^{\frac{i\Phi}{2}} & 0 \\ 0 & e^{-\frac{i\Phi}{2}} \end{bmatrix} \begin{bmatrix} H_1' & H_2' \\ V_1' & V_2' \end{bmatrix} \begin{bmatrix} H_1 & e^{i\alpha} H_2 \\ V_1 & e^{i\alpha} V_2 \end{bmatrix}^{-1} \begin{bmatrix} e^{-\frac{i\Phi}{2}} & 0 \\ 0 & e^{\frac{i\Phi}{2}} \end{bmatrix} \begin{bmatrix} \cos\Theta & -\sin\Theta \\ \sin\Theta & \cos\Theta \end{bmatrix} \tag{1.21}$$

The parameters describing diattenuation, phase retardance and the orientation of the optic axis can be determined simultaneously by minimizing the sum of the magnitudes of the off-diagonal elements of the matrices on the right hand side. The Jones matrix based method is convenient due to the fact that multiple polarization parameters can be simultaneously extracted from a sample and separate measurements are not needed.

Section 1.3.2: Stokes vector based method

The Stokes vector based method is a convenient formalism to use when describing depolarizing phenomena and incoherent addition of light. An additional way of describing the electric field components of polarized light is with a real 4-element vector called a Stokes vector:

$$S = \begin{bmatrix} I \\ Q \\ U \\ V \end{bmatrix} = \begin{bmatrix} E_{\|}\tilde{E}_{\|} + E_{\perp}\tilde{E}_{\perp} \\ E_{\|}\tilde{E}_{\|} - E_{\perp}\tilde{E}_{\perp} \\ E_{\|}\tilde{E}_{\perp} - E_{\perp}\tilde{E}_{\|} \\ i\left(E_{\|}\tilde{E}_{\perp} - E_{\perp}\tilde{E}_{\|}\right) \end{bmatrix} \tag{1.22}$$

These real 4-element Stokes vectors can be related to one another using 4x4 matrices known as Mueller matrices. These matrices can be used to describe the polarization properties of any depolarizing material. A transmitted polarization state S' can be described by the effects on an incident polarization state S after traveling through material defined by a Mueller matrix M:

$$S' = \begin{bmatrix} I' \\ Q' \\ U' \\ V' \end{bmatrix} = \begin{bmatrix} M_{11} & M_{12} & M_{13} & M_{14} \\ M_{21} & M_{22} & M_{23} & M_{24} \\ M_{31} & M_{32} & M_{33} & M_{34} \\ M_{41} & M_{42} & M_{43} & M_{44} \end{bmatrix} \begin{bmatrix} I \\ Q \\ U \\ V \end{bmatrix} = MS \tag{1.23}$$

where M represents the 4x4 Mueller matrix of the depolarizing material, S is the incident Stokes vector and S' is the transmitted Stokes vector. If the incident polarization state S travels through a series of n materials, each described by a unique Mueller matrix M_n, the transmitted state S' is described by the combined effects of the Jones matrices M_n acting on the incident state S, i.e. $S' = (M_n \dots M_2 M_1)S$.

Unique Mueller matrices exist to describe dichroic and birefringent materials. Following the notation from Park [27], the Mueller matrix for a dichroic material with attenuation ratios P_1 and P_2 and an optic axis orientation described by θ and ϕ can be described as follows:

$$M_d = \begin{bmatrix} q_1 & q_2\cos 2\theta & q_2\sin 2\theta\cos\phi & q_2\sin 2\theta\sin\phi \\ q_2\cos 2\theta & q_3+(q_1-q_3)\cos^2 2\theta & (q_1-q_3)\cos 2\theta\sin 2\theta\cos\phi & (q_1-q_3)\cos 2\theta\sin 2\theta\sin\phi \\ q_2\sin 2\theta\cos\phi & (q_1-q_3)\cos 2\theta\sin 2\theta\cos\phi & q_3+(q_1-q_3)\sin^2 2\theta\cos^2\phi & (q_1-q_3)\sin^2 2\theta\cos\phi\sin\phi \\ q_2\sin 2\theta\sin\phi & (q_1-q_3)\cos 2\theta\sin 2\theta\sin\phi & (q_1-q_3)\sin^2 2\theta\cos\phi\sin\phi & q_3+(q_1-q_3)\sin^2 2\theta\sin^2\phi \end{bmatrix} \tag{1.24}$$

where $q_1 = \frac{1}{2}(P_1^2 + P_2^2)$, $q_2 = \frac{1}{2}(P_1^2 - P_2^2)$ and $q_3 = P_1P_2$. The Mueller matrix describing birefringent materials follows a similar form. For a given phase retardance η between orthogonal polarization states and an optic axis orientation and circularity described by Θ and Φ respectively, the Mueller matrix for birefringence can be described by the following equation:

$$M_b = \begin{bmatrix} 1 & 0 & 0 & 0 \\ 0 & \cos\eta+(1-\cos\eta)\cos^2 2\Theta & -\sin\eta\sin 2\Theta\sin\Phi+(1-\cos\eta)\cos 2\Theta\sin 2\Theta\cos\Phi & -\sin\eta\sin 2\Theta\cos\Phi+(1-\cos\eta)\cos 2\Theta\sin 2\Theta\sin\Phi \\ 0 & -\sin\eta\sin 2\Theta\sin\Phi+(1-\cos\eta)\cos 2\Theta\sin 2\Theta\cos\Phi & \cos\eta+(1-\cos\eta)\sin^2 2\Theta\cos^2\Phi & \sin\eta\cos 2\Theta+(1-\cos\eta)\sin^2 2\Theta\cos\Phi\sin\Phi \\ 0 & -\sin\eta\sin 2\Theta\cos\Phi+(1-\cos\eta)\cos 2\Theta\sin 2\Theta\sin\Phi & -\sin\eta\cos 2\Theta+(1-\cos\eta)\sin^2 2\Theta\cos\Phi\sin\Phi & \cos\eta+(1-\cos\eta)\sin^2 2\Theta\sin^2\Phi \end{bmatrix} \tag{1.25}$$

In most biological tissue, the dominant polarization effect exhibited is birefringence. Under the assumption that diattenuation in negligible, a simplified Stokes vector-based method can be used to determine the birefringence of biological samples. In the simplified Stokes vector-based method, the polarization state of the light reflected back from the sample surface is compared to the polarization state of light reflected back

from depths within the tissue for two incident polarization states orthogonal in a Poincare sphere representation. The Stokes vector representation of the polarization state of light reflected back from a given depth within the tissue can be described by the following equation:

$$S_n(z_m) = \begin{bmatrix} Q_n(z_m) \\ U_n(z_m) \\ V_n(z_m) \end{bmatrix} = \begin{bmatrix} H_n(z_m)\cdot\tilde{H}_n(z_m) - V_n(z_m)\cdot\tilde{V}_n(z_m) \\ H_n(z_m)\cdot\tilde{V}_n(z_m) + \tilde{H}_n(z_m)\cdot V_n(z_m) \\ i\left(H_n(z_m)\cdot\tilde{V}_n(z_m) - \tilde{H}_n(z_m)\cdot V_n(z_m)\right) \end{bmatrix} \tag{1.26}$$

where n is the A-line number, z_m is the depth and H and V represent the orthogonal electric field components detected by a polarization-sensitive spectrometer. These Stokes vectors are averaged over an area corresponding to the spatial resolutions of the system and normalized to yield the following:

$$N_n(z_m) = \left(\sum_{\delta x, l_c} S_n(z_m)\right) \Big/ \left|\sum_{\delta x, l_c} S_n(z_m)\right| \tag{1.27}$$

where δx represents the lateral beam diameter incident on the tissue and l_c is the coherence length of the source. The surface of the tissue sample was determined by median filtering and thresholding. The cumulative sample optic axis that simultaneously rotates a pair of polarization states at the surface to those at a particular depth can be described as:

$$A_p(z_m) \parallel \left(N_{2p}(s_{2p}) - N_{2p}(z_m)\right) \times \left(N_{2p+1}(s_{2p+1}) - N_{2p+1}(z_m)\right) \tag{1.28}$$

where A_p is the sample optic axis and p denotes the electric field component (horizontal or vertical). The phase retardance angle required to rotate the surface polarization state to

the polarization state from a particular depth around the sample optic axis for each of the two orthogonal incident polarization states is given by the following two equations:

$$\theta_{2p}(z_m) = \cos^{-1}\frac{\left|\left(A_p(z_m)\times N_{2p}(s_{2p})\right)\cdot\left(A_p(z_m)\times N_{2p}(z_m)\right)\right|}{\left|A_p(z_m)\times N_{2p}(s_{2p})\right|\left|A_p(z_m)\times N_{2p}(z_m)\right|} \tag{1.29}$$

$$\theta_{2p+1}(z_m) = \cos^{-1}\frac{\left|\left(A_p(z_m)\times N_{2p+1}(s_{2p+1})\right)\cdot\left(A_p(z_m)\times N_{2p+1}(z_m)\right)\right|}{\left|A_p(z_m)\times N_{2p+1}(s_{2p+1})\right|\left|A_p(z_m)\times N_{2p+1}(z_m)\right|} \tag{1.30}$$

The final overall phase retardance angle can be computed as the average of the two phase retardance angles computed in (1.29) and (1.30).

Section 1.4: Doppler optical coherence tomography (D-OCT)

Doppler optical coherence tomography (D-OCT) is a functional extension of OCT imaging used to perform high-resolution mapping of fluid flow within biological tissues [28,29,30,31,32]. Light scattered back from moving particles in a given fluid induces a frequency shift (the Doppler effect) in the detected interference pattern that is proportional to the velocity of the fluid. An additional method for obtaining flow velocity information is by examining the phase shifts of the back scattered light waves in areas of flow. Phase-resolved D-OCT uses the phase changes between sequential scans to reconstruct images of fluid flow [33]. Phase information can be extracted from the complex-value A-line (1.8) resulting from the Fourier transform of the spectral interferogram. For two camera SD-PS-OCT systems, phase differences between sequential scans with the same incident polarization state are computed:

$$\Delta\phi_{H_n,V_n}(z_m) = \phi_{H_n,V_n}(z_m) - \phi_{H_{n-2},V_{n-2}}(z_m) \tag{1.31}$$

Two types of flow images can be reconstructed based on these phase differences: bi-directional [33] and phase variance images [34]. In both cases, the overall phase shift between sequential scans is corrected for. The intensity-weighted averages of the phase differences are calculated and used to improve the quality of the image due to the dependence of phase noise on SNR [35]. Bi-directional flow images are generated by computing the intensity-weighted average phase difference:

$$\omega_n(z_m) = \frac{1}{2T}\frac{|H_n(z_m)|^2 \Delta\phi'_{H_n}(z_m) + |V_n(z_m)|^2 \Delta\phi'_{V_n}(z_m)}{|H_n(z_m)|^2 + |V_n(z_m)|^2} \tag{1.32}$$

where $H_n(z_m)$ and $V_n(z_m)$ are the intensities of the two cameras respectively, $\Delta\phi'_{H_n}(z_m)$ and $\Delta\phi'_{V_n}(z_m)$ are the phase differences of sequential scans with the same incident polarization state and T is the time between sequential scans. The values of the phase differences range from $-\pi$ to $+\pi$ and inform us of the direction of flow. Phase variance images are generated by computing the intensity-weighted average of the square of the phase difference:

$$\sigma_n^2(z_m) = \frac{|H_n(z_m)|^2 \Delta\phi'^2_{H_n}(z_m) + |V_n(z_m)|^2 \Delta\phi'^2_{V_n}(z_m)}{|H_n(z_m)|^2 + |V_n(z_m)|^2} \tag{1.33}$$

The values of the square of the phase difference range from 0 to π^2 and inform us of the presence of flow only. This type of flow information is well-suited for reconstruction of high-resolution structural images of fluid flow.

Chapter 2: High speed multi-functional spectral-domain optical coherence tomography using graphics processing units (GPUs)

This chapter describes the development and implementation of parallelized multi-functional spectral-domain optical coherence tomography processing algorithms for accelerated 2D and 3D visualization of imaging data. The chapter is organized into four main sections: an introduction and comparison of serial and parallel computing architectures (Section 2.1), descriptions of NVIDIA CUDA and the CUDA programming model (Sections 2.2 and 2.3) and finally, the details of the implementation of the parallelized multi-functional spectral-domain optical coherence tomography processing algorithms accompanied by demonstrations of the performance improvements obtained over serialized processing algorithms for two-dimensional and three-dimensional data (Sections 2.4 and 2.5).

Early implementations of accelerated data processing were done using field programmable gate array (FPGA) integrated circuits and custom electronics boards [36,37,38,39]. A-line processing rates of ~28 kHz and 54 kHz were achieved for SD-OCT [38] and swept-source OCT [39] systems respectively. Implementation of FPGA-based processing can be complex and expensive and doesn't allow the acquired raw data to be saved for off-line processing. More recently, GPUs have been employed for high-speed general purpose computation. GPU-based solutions tend to be less complex and less expensive compared to their FPGA counterparts and still allow raw data to be saved for off-line processing. A-line processing rates of more than 500 kHz have been demonstrated using GPUs for computation [40,41]. Additionally, GPU-accelerated

implementations of Doppler OCT processing have been reported by other groups and a GPU-accelerated implementation of MF-SD-OCT processing has been reported by our group [44]. A high-speed MF-SD-OCT system enables rapid structural and functional assessment of biological samples and monitoring of fast dynamic biological phenomena across all three spatial dimensions.

Section 2.1: Serial vs. parallel computing paradigms

A central processing unit, or CPU, is the hardware contained inside of a computer that is tasked with carrying out the instruction sets of computer programs. These instructions sets can be comprised of input/output operations to/from memory and arithmetic and logical operations. At its simplest form, CPUs contain two basic components: arithmetic logic units (ALUs) and control units (CUs). ALUs are responsible for carrying out arithmetic and logical operations and CUs are responsible for extracting and executing instructions from memory. CPUs are contained on a single chip and comprised of many small semiconductor devices called transistors. Single chips can have multiple CPUs on them and are the basis for the multi-core CPUs we see in PCs today.

CPUs execute tasks using a small number of resource-heavy threads executed by one or more cores. Similarly, these threads handle computation on large arrays in a serial fashion. This results in repetitive work being done by resource-heavy threads and begins to become computationally expensive and time inefficient. The simplest solution is to divide up the work over multiple threads and run them in parallel to remove some of the

redundancy. However, multi-core CPUs can only launch a small number of threads due to the limited number of cores and significant overhead in their creation.

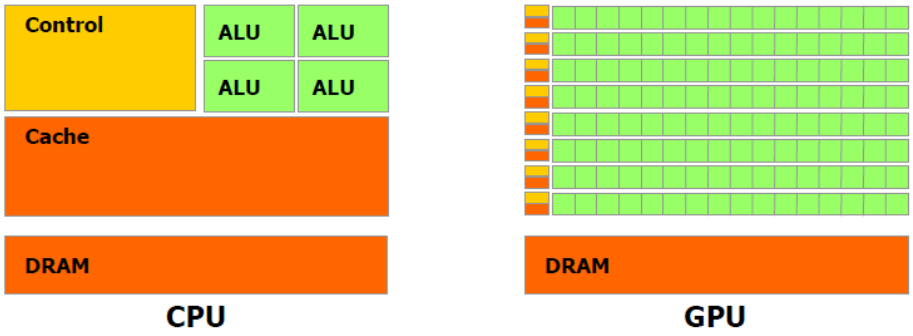

Figure 2.1: Serial vs. parallel hardware schematics [42]. GPUs commit more physical space to computational units compared to CPUs. ALU: arithmetic logic unit, DRAM: dynamic random access

Graphics processing units (GPUs) are specialized processors that have been designed and optimized for handling the large computational workloads that accompany the processing and rendering of graphics to displays in modern PCs. They allocate much of their physical space on chip to cores dedicated to performing computation. While modern CPUs may contain six to eight cores, GPUs can have hundreds to thousands of cores on chip (Figure 2.1). This enables the GPU to launch hundreds to thousands of lightweight threads to execute tasks and computation in a highly parallelized and time efficient manner. In addition to the cores, GPUs have additional physical space dedicated to device random access memory (DRAM) used for storing data to be manipulated by the cores. These properties make the GPU an ideal co-processor to the CPU.

The biggest advantage offered by GPUs and parallel computing is that the large numbers of cores present on the GPU allows for handling large amounts of data in a parallel and computationally efficient manner. Due to the co-processor nature of the

GPU, the CPU can offload data to the DRAM on the GPU for parallel processing while continuing to execute the instruction set of the scheduled program. Implementation of parallelized computation was largely restricted to developers with a graphics and visualization background due to the lack of a general purpose programming platform for leveraging the parallel computing hardware of the GPU. It wasn't until the release of the CUDA programming platform by NVIDIA that implementations of general purpose parallelized computation became widely available.

Section 2.2: NVIDIA Compute Unified Device Architecture (CUDA)

In 2006, NVIDIA released a parallel computing platform and programming model named CUDA to leverage the power of GPUs for enhanced computing performance. CUDA enables parallel computing support for all developers from all walks of science and engineering with three possible approaches: (1) GPU-accelerates libraries of functions to replace or modify CPU library analogs, (2) automatic parallelization of loops using OpenACC and (3) providing a platform for developing custom parallelized algorithms and libraries by providing a language that extends industry standard languages like C, C++ and Fortran. These keep the learning curve for parallel programming low and allow current programmers to take advantage of parallel computing for their own applications. In addition to a low learning curve, developers can take advantage of hardware scalability of their developed algorithms. Algorithms developed on past generations of hardware scale to future generations of hardware due to the programming and execution models it implements. The CUDA platform and programming model have

been used by developers across a wide variety of disciplines to accelerate their code by orders of magnitude compared to their CPU counterparts. It is a truly transformative technology development platform that has enabled the accessibility of high performance computing on graphics processing units (GPUs) to developers working on more general-purpose applications and solutions.

Section 2.3: CUDA Programming Model

The CUDA programming model is a scalable programming model designed to transparently scale its parallelism across devices with variable numbers of processing cores while maintaining a low learning curve for programmers and developers [42]. The main concepts that comprise the model are kernels, the thread hierarchy and the memory hierarchy. This model enables developers to take advantage of hybrid CPU-GPU computing to increase the performance and computational efficiency of their applications.

Section 2.3.1: The CUDA kernel

At the heart of the CUDA programming model is the kernel. Kernels are C functions that are run many times in parallel by an array of threads on a GPU. This is in contrast to CPU-executed C functions, which occurs only once. The arrays of threads concurrently launched by the GPU to execute the kernel can be programmatically defined and is limited by the physical hardware of the GPU. Kernels are invoked with a specific

syntax that defines the numbers of threads and blocks and the input and output arguments to the kernel. The kernel invocation syntax is as follows:

KernelFunc<<<BlocksPerGrid,ThreadsPerBlock>>>(FuncArgs), where *BlocksPerGrid* and *ThreadsPerBlock* defined the grid size and block size respectively, and *FuncArgs* defines the inputs and outputs to the kernel [42]. The arrays of threads launched to execute the kernel are arranged into a specialized hierarchy to facilitate the management and scheduling of these threads to execute the kernel on the device. Execution of different hierarchical groups is associated with specific hardware components on the GPU.

Section 2.3.2: The thread hierarchy

At the lowest level of the thread hierarchy is the thread, sometimes referred to as a CUDA thread. When a kernel is launched on the device, a large array of threads is launched to execute the kernel. CUDA threads are extremely light weight compared with CPU threads and therefore, do not require significant resources to launch large numbers of them. On the hardware side, CUDA threads are executed by the streaming processors (SP) of a given streaming multiprocessor (SM) on a GPU. On the software side, each CUDA thread in uniquely identified by a built-in multi-dimensional ID variable that is used to compute memory addresses and make control decisions. The *threadIdx.x, threadIdx.y* and *threadIdx.z* variables describe the 3-space coordinates for a given thread within a block [42].

At the second level of the thread hierarchy is the block. Blocks serve to divide up the large array of CUDA threads that are launched during kernel execution. On the hardware side, blocks are executed by SM's on a compute device. The hardware is free to assign the execution of blocks to any SM at any time, providing transparent scalability across GPUs of different generations. The generation of the GPU dictates the maximum number of threads per block due to the execution of all threads in a block being done by the same SM. Threads within a given block can cooperate via a special memory space called Shared Memory (Figure 2.2). A detailed description of Shared Memory is provided below. On the software side, each block and its dimensions are uniquely identified by built-in multi-dimensional ID variables. The *blockDim.x* and *blockDim.y* variables describe the lengths and widths (in numbers of threads) of a given block respectively [42]. The *blockIdx.x* and *blockIdx.y* variables describe the position of a given block inside of a grid of blocks [42]. The number of threads per block can be programmatically defined at kernel launch with the kernel invocation syntax.

Finally, at the top of the thread hierarchy is the grid. The grid is a multi-dimensional array of thread blocks that is launched during kernel invocation. On the hardware side, a grid is executed across all the SMs of a given GPU. The blocks within a grid are assigned to SMs and the threads within a block are assigned to the SPs within a given SM. Blocks within a grid can cooperate via a special memory space called Global Memory (Figure 2.2). A detailed description of Global Memory is described below. On the software side, the dimensions of a grid can be accessed via built-in multi-dimensional ID variables. The *gridDim.x* and *gridDim.y* variables describe the length and width of a

grid respectively [42]. The number of blocks per grid can be programmatically defined at kernel launch within the kernel invocation syntax.

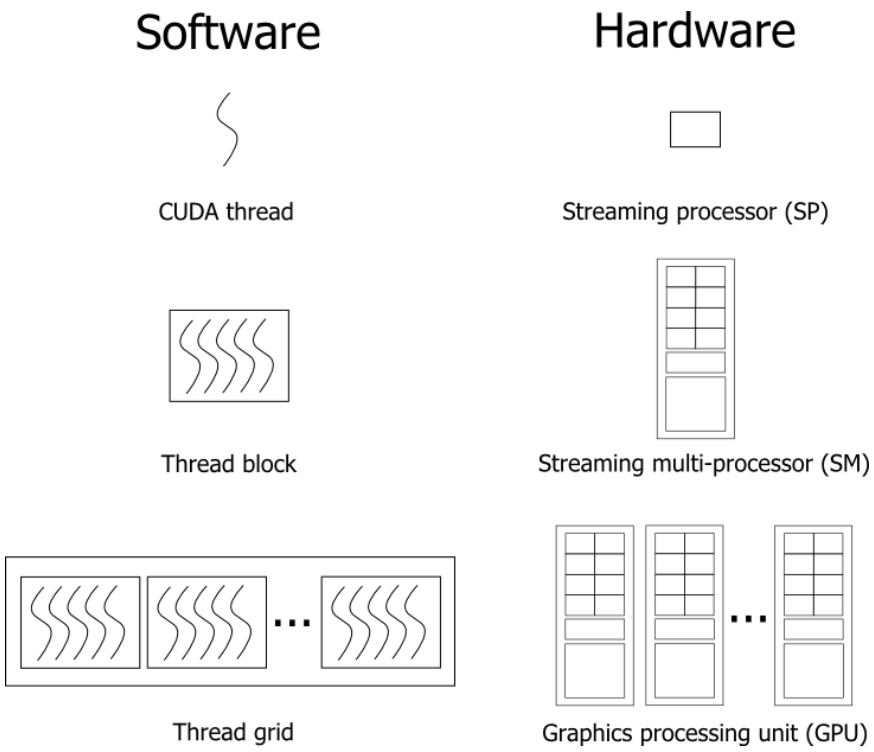

Figure 2.2: Hardware and software association within the CUDA programming model. CUDA threads are executed via streaming processors (SP), blocks of CUDA threads are executed on streaming multiprocessors (SM) and grids of blocks of CUDA threads are executed across the multiple SMs on a GPU.

Section 2.3.3: The memory hierarchy

The CUDA programming model consists of multiple memory spaces available for developers to use. Effective use of these special memory spaces is crucial to achieving speedups in computation time and improvements in computational efficiency. Each memory space has its own read/write latencies and a specific association with one of the levels of the thread hierarchy. This results in each memory space being well-suited for

particular read/write patterns and computational tasks. The main memory spaces available to the developer in the CUDA programming model are constant, texture, shared and global memory spaces and will be discussed below.

Constant and texture memory are special read-only memory spaces. They are accessible by all threads and blocks on a given GPU. The constant memory space derives its name from the fact that this memory space should store data that will persist throughout the lifetime of the application. Read operations from this memory space only takes a few clock cycles, making this space well suited for reading reference-type data frequently. Texture memory is optimized for data that has some 2D locality to it and can enable better performance if memory reads do not follow access pattern regulations required by other memory spaces.

The best memory space to exploit for performance gains when developing GPU kernels is Shared Memory. The shared memory space is an on-chip memory space accessible to all threads in a given block. The read/write latencies to this memory space are extremely low; on the order of a few clock cycles. This makes the shared memory space well suited for performing frequent computations and data read/write operations. However, the shared memory space capacity is small in comparison to other CUDA memory spaces. Each generation of GPU has an upper limit on the amount of shared memory per block that can be allocated and used and typically reaches capacities on the order of tens of kilobytes. This forces developers to develop strategies for caching data in shared memory as needed while minimizing the number of read/write operations to more temporally expensive memory spaces.

Global memory is the largest of the CUDA memory spaces with capacities into the gigabyte range. This memory space is the primary memory space involved in host-device data transfers. Data prepared for CUDA-based processing is transferred to the GPU and stored in global memory. Once CUDA-based processing has completed, the output is written to global memory for transfer back to the host. Global memory is also used to hold large amounts of data that are unable to fit into other CUDA memory spaces. It is visible to all threads across a GPU and can be used for data cooperation between threads and blocks. However, reading and writing to this memory space can be temporally expensive due to the long latencies associated with accessing it. These latencies are on the order of a few hundred clock cycles, which necessitates the minimization of read and write operations to this memory space when developing kernels for efficient, high-performance GPU computing.

Section 2.3.4: Heterogeneous/hybrid computing

The concepts of kernels and thread and memory hierarchies describe how CUDA enables the GPU to act as co-processor to the CPU. The integration of CUDA code into C-based applications is the idea behind heterogeneous or hybrid computing. Data is prepared for processing in the host memory space by the CPU, transferred to the GPU memory space for CUDA processing and transferred back to the host memory space for output or display. Because of the special syntax used for GPU computing, it is unable to be compiled by the standard gcc compiler. Instead, CUDA provides the nvcc compiler designed to compile CUDA code. To use nvcc to compile CUDA code, the code must be

written in files with special extensions to distinguish it from code compiled with gcc. The .cuh and .cu file extensions denote CUDA header and implementation files respectively and indicate that they should be compiled using nvcc.

Once the host and device code is placed into its respective files, special C functions called wrappers must be written to allow the host to call on the developed GPU kernels. A wrapper function is a function with a C-based front end to allow it to be called from the host but executes device functions or kernels on the GPU. These types of functions are written into .cu files for compilation by nvcc but can be used within any C-based implementation file. Any device function or kernel can be written into a wrapper function and executed within a C-based implementation file. Once the appropriate wrappers are written, they can be used in any C-based application to handle the execution of CUDA device functions and kernels. The result is a hybrid application that should boast superior performance compared with its serial counterpart (Figure 2.3).

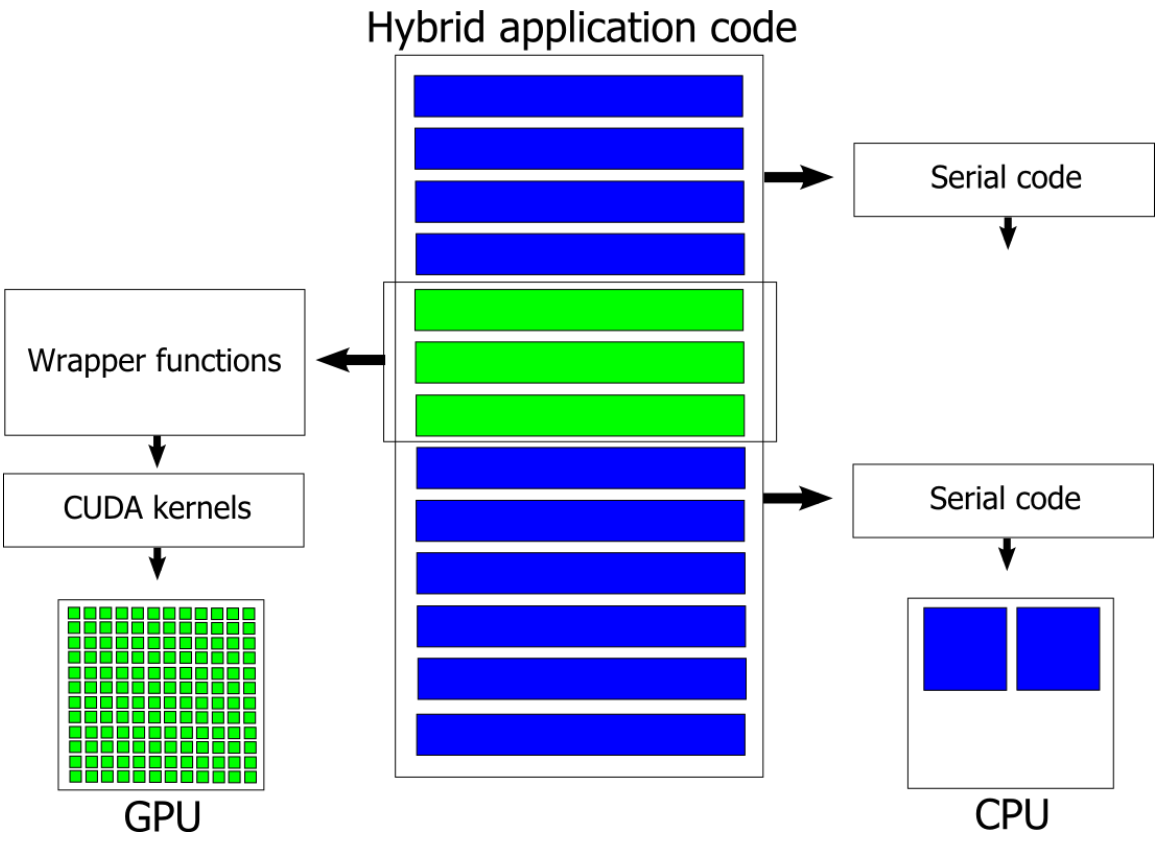

Figure 2.3: Hybrid CPU/GPU computing diagram. Serialized code is executed on the CPU and parallelized code is executed on the GPU by calling C-based wrapper functions which invoke CUDA kernels.

Section 2.4: Multi-functional spectral-domain optical coherence tomography on CUDA-enabled GPUs

The data stream into a PC acquired by a multi-functional spectral-domain OCT system can be substantial. Data streams can be upwards of 1 GB/sec for a top of the line PS-OCT-based spectrometer equipped with two 8-bit 1024-pixel spectrometers operating at 500 kHz. Significant computing power is needed to process this data stream into 2D and 3D images for visualization and analysis. A software application capable of processing the multi-functional spectral-domain OCT data stream is real time would have

significant research and clinical utility. Our solution for achieving this computational capability was to leverage the power and parallel processing architecture of GPUs by using the CUDA parallel programming platform to design and implement GPU-accelerated multi-functional spectral-domain OCT data processing algorithms. We developed 2D multi-functional spectral-domain OCT data processing algorithms and methods for visualization of 3D multi-functional OCT data. These algorithms and methods were integrated into our prior multi-threaded software application for managing the acquisition, processing and saving of multi-functional spectral-domain OCT data [43]. The result is a hybrid computing software application with enhanced processing speeds and extended data visualization functionality due to GPU-based computation. The multi-functional spectral-domain OCT data stream is processed in real-time using CUDA and the extended 3D data visualization functionality is handled by the OpenGL framework [44]. The utility of the software application was demonstrated using a custom-built polarization-sensitive spectral-domain OCT system centered at 1300 nm to acquire, process, display and save multi-functional OCT images from multiple biological samples in real-time (Figure 2.4).

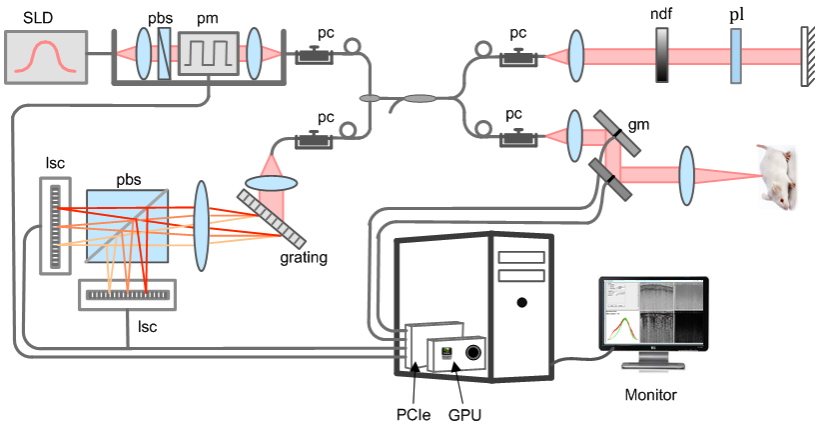

Figure 2.4: System diagram of the multi-functional spectral-domain OCT imaging system centered at 1300 nm. SLD: superluminescent diode, pbs: polarization beam splitter, pm: polarization modulator, pc: polarization controller, ndf: neutral density filter, pl: polarizer, gm: galvo mirror, lsc: line scan camera, PCIe: PCI express, GPU: graphics processing unit.

The broadband source is composed of two super-luminescent diodes (SLD), one centered at 1295nm with a full-width at half maximum (FWHM) bandwidth of 97nm and the other centered at 1350nm with a FWHM bandwidth of 48nm. The resulting source is centered at 1298nm with a 120 nm FWHM bandwidth and 16mW power. Light from the source is collimated and passes through a polarizing beam splitter (pbs) and a polarization modulator (pm) that toggles the light between two orthogonal polarization states in a Poincaré sphere representation. The polarized light is sent to a fiber circulator and an 80/20 fiber splitter with a polarization controller (pc). In the reference arm, a neutral density filter (ndf) is used to adjust light reflecting from the reference mirror, and a polarizer (pl) is used to insure uniformity of the reference polarization state. In the sample arm, galvanometer mounted mirrors in the hand-piece provide transverse scanning of a 10 micron diameter focused spot. Light from both arms is recombined in the splitter and passes through a transmission diffraction grating (1100 lines per mm)

before being focused by a planoconvex lens. The two polarization states of light are separated by a polarizing beam splitter and collected by two line scanning cameras (lsc) separately with readout rates up to 45 kHz. Output from the two cameras is digitized through two National Instruments frame grabber boards (PCIe NI-1429). The cameras, galvanometer mirrors and polarization modulator are triggered by synchronized signals sent from the computer via a National Instruments data acquisition board (PCIe NI-6259). The GPU used for data processing is the NVIDIA Tesla C1060 card connected via a PCIe 2.0 x16 interface. The NVIDIA Tesla C1060 has 240 cores with a core clock speed of 1.296 GHz, 4GB physical memory and memory clock speed of 800 MHz. The computer CPU is an Intel Xeon W5580, which has two cores with clock speed of 3.2 GHz.

The multi-threaded application was developed using Microsoft Visual Studio 2008 and written using Visual C++ and MFC. Separate threads parallelize and synchronize program operation. One thread synchronizes the line scan cameras, galvanometer-mounted mirrors and polarization modulator while other threads acquire the data stream from the line scan cameras, process and display the data stream to the graphical user interface (GUI) and save the data stream down to the hard drive for post-processing and analysis. The GUI is comprised of a control panel to handle system operation and multiple views to display the spectra on the line scan cameras and the intensity, polarization-sensitive, Doppler and *en face* OCT cross-section and volumetric images.

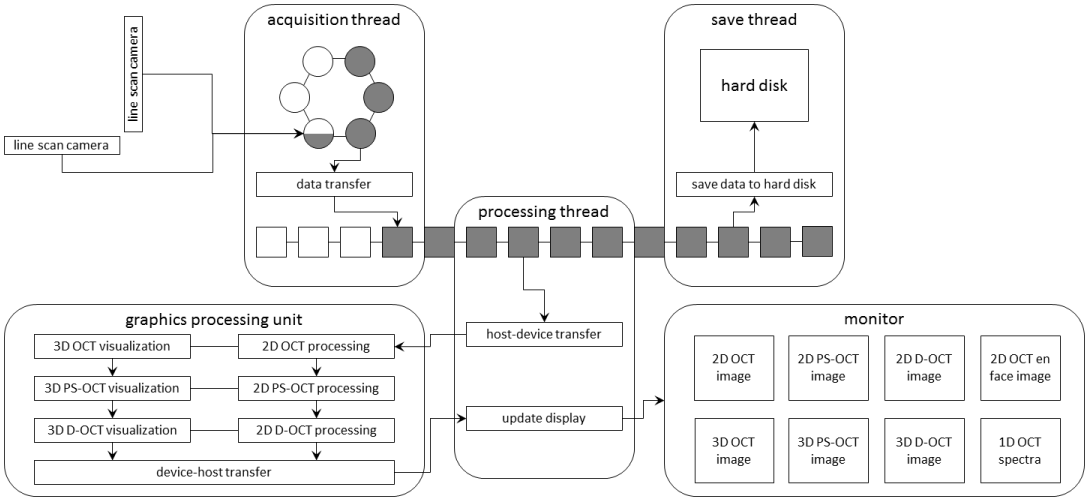

Figure 2.5: Diagram of the operation of the multi-threaded software application for handling the acquisition, GPU-accelerated processing, saving and visualization of 2D and 3D multi-functional OCT data.

The multi-threaded base structure of the software application facilitated the integration of our GPU-accelerated data processing algorithms. A single thread was dedicated to the processing of the OCT data stream using the Intel Performance Primitives (IPP) library. We thoroughly analyzed our current OCT data processing algorithms to determine which computational steps in the workflow would benefit from parallel processing. As a general rule, any operations that have no dependency on the outcomes of other operations can be parallelized. Element-wise operations on arrays contained within for-loops are prime examples of computational steps that can be parallelized. The nature of OCT acquisition and processing make it well-suited for parallel processing. The acquisition of each A-line from the line scan cameras in the spectrometer is done independently. Our software application acquires and stores a user-defined number of A-lines corresponding to a B-line in internal data storage structures.

The independence of A-line acquisition means we can process all the A-lines from the internal data storage structure in parallel and assemble them into a B-line after the processing has completed. Additionally, there are numerous computational steps in the multi-functional OCT processing work flow that require element-wise operations for image reconstruction. Given that A-lines are arrays of data and element-wise operations on arrays are well suited for parallel processing, we get processing performance enhancement by parallelizing these computational steps. These ideas guided our developed of custom CUDA kernels to process the multi-functional spectral-domain OCT data stream in real-time. With the savings in processing time due to parallel computation, we implemented OpenGL-based 3D data visualization methods. The IPP-based processing in the thread was replaced by the CUDA-based OCT data processing algorithms with the addition of the OpenGL-based 3D data visualization methods.

On application startup, both host and device initialization procedures are executed. Host initialization procedures include loading of the camera calibration files and wavelength-to-wavenumber resampling needed for interpolation procedures, thread setup and initialization, camera setup and initialization and general memory allocations for core data structures. Device initialization procedures include device memory allocations for computation data structures, plan creation for CUDA-based fast Fourier transform using the CUFFT library [45], computation of a reference model-view matrix for 3D visualization using OpenGL and transfer of the pre-computed interpolation arrays to the device. During application runtime, raw OCT spectral data is copied to the GPU and converted from 16-bit unsigned integers to 32-bit floating point values. The average

spectrum of all A-lines in a given image is computed and subtracted away from each A-line separately. The spectra is then linearly interpolated [40] and Fourier transformed [45], resulting in a processed, complex-data B-line. The B-line intensity values are converted to a log scale and rescaled for 8-bit grayscale display. These complex-data B-lines are used in PS-OCT and Doppler-OCT computations of Stokes-vector-based phase retardance and bi-directional- and phase variance-based flow respectively. The phase retardance values are rescaled for 8-bit grayscale display where black represents black representing zero degrees of phase retardance and white represents 180 degrees of phase retardance. Bi-directional flow values are rescaled for 8-bit grayscale display where black represents $-\pi$, gray represents zero and white represents $+\pi$ phase values. Phase variance values are rescaled for 8-bit grayscale display where black represents zero and white represents π^2 variance values (Figure 2.6).

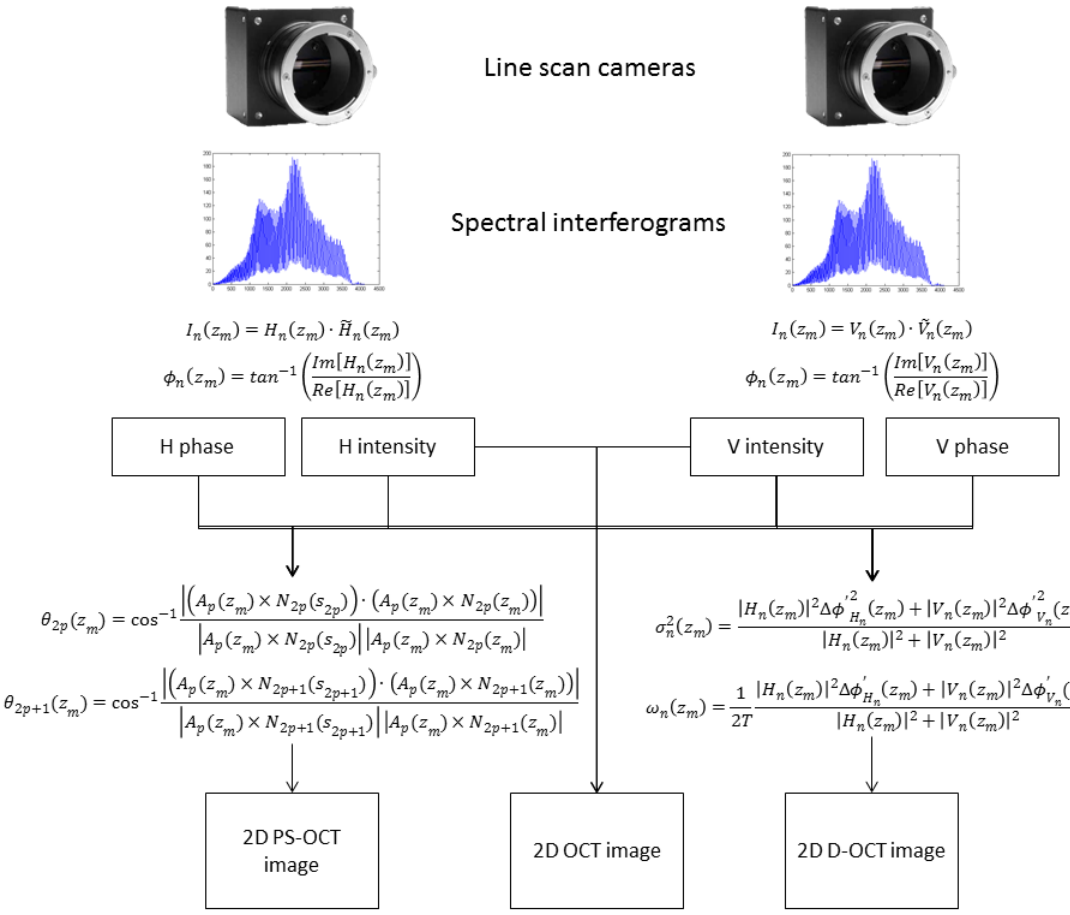

Figure 2.6: Mathematical work flow of 2D MF-SD-OCT processing on the GPU.

Finally, an *en face* OCT image is generated from any of the three types of OCT images based on user selection of an image depth and image type. Once a volume of data has been processed for intensity, phase retardance and flow, these data are copied to a 3D texture memory space on the GPU. A model-view matrix is used to transform the volumetric data from model space to view space using inputs from peripheral devices. These transformed data are rendered using volumetric ray casting and stored in a pixel buffer object. Finally, the contents from the pixel buffer object are copied back to texture

memory for display in the OpenGL based views. Once all computation has been completed, the average spectra and processed images are transferred back to the host for display (Figure 2.5).

Section 2.4.1: Two-dimensional GPU-accelerated OCT processing

The performance enhancement of two-dimensional multi-functional OCT imaging using CUDA-based processing is demonstrated by imaging the structure of the lateral eye of the horseshoe crab, the progression of thermal damage due to localized heating of chicken muscle tissue, pulsed fluid flow through a microfluidic device and the mouse cortex *in vivo*. This is visualized with video recordings of the GUI of the software application during acquisition of images from the aforementioned samples. Performance enhancement is measured by comparing the execution times of CPU-based computation with that of the CUDA-based computation. CPU execution times were measured using the *QueryPerformanceCounter()* and *QueryPerformanceFrequency()* functions provided by Microsoft. GPU execution times were measured using event management within the CUDA Runtime API [42]. Speedups were calculated by taking the ratio of GPU execution times to CPU executions time for the same processing tasks. First, to determine the minimum number of A-lines per image necessary to see a performance enhancement for multi-functional OCT imaging, the number of A-lines per image was varied and the CPU and GPU computation times for a single image were measured and compared (Figure 2.7).

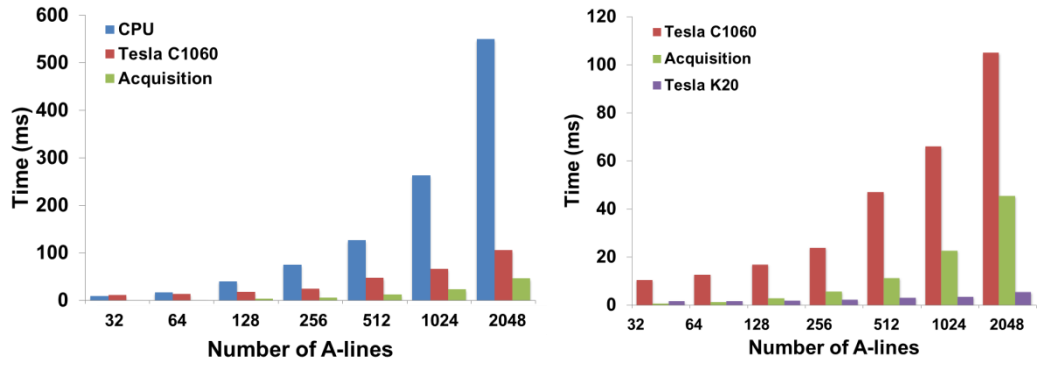

Figure 2.7: Processing times for a single frame plotted against number of A-lines in a frame. Initial work demonstrated speedups of 5x for GPU-based computation compared to CPU-based computation. Optimization of the kernels and the installation of the NVIDIA Tesla K20 increased the speedup to 100x and decreased the GPU-based computation time to less than the acquisition time for a single frame for all image sizes.

As the number of A-lines in an image increases, the performance enhancement of GPU computation becomes more pronounced. This data demonstrates the minimum number of A-lines in an image required to begin seeing a performance enhancement due to GPU computation is 128 for multi-functional OCT processing. However, in all cases, the GPU-based computation times still exceeded the image acquisition times of the system running at full speed. By optimizing the execution of the kernels and installing the NVIDIA Tesla K20 GPU, the GPU-based computation times became faster than the image acquisition times for all image sizes and a 100x speedup over CPU-based computation was realized (Figure 2.7). Next, the computation times for each of the OCT modalities was calculated and compared to determine at which step the most significant speedup occurred. The time to transfer data between the host and device memory spaces was included in the total GPU computation time to accurately determine performance enhancement. The performance enhancement is especially evident in PS-OCT and Doppler OCT processing

due to the replacement of multiple nested for-loops with parallelized computation (Table 2.1).

Table 2.1: Comparison of computation times for CPU-based and GPU-based processing and the speedup obtained.

Task	CPU (ms)	GPU (ms)	Speedup
Copy from buffer to CPU	12	12	1
Copy between CPU and GPU	0	22	-
Compute intensity	55	10	5.5
Compute phase retardance	392	25	15.68
Compute flow	549	12	45.75
Display	25	25	1
Total	641	106	6.04717

Demonstration of the performance enhancement that GPU computation provides is best shown with video recordings of the increased processing speeds. The addition of extra OCT imaging modalities increases the total computation time but still exhibits a speedup compared with the CPU computation time. In all cases, the spectral-domain multi-functional OCT imaging system is run at its max speed of 45 kHz.

First, to demonstrate GPU-accelerated OCT intensity imaging, three differently sized volumetric images (12,800 A-lines/volume; 256 A-lines/frame x 50 frames/volume x 512 points/A-line, 25,600 A-lines/volume; 512 A-lines/frame x 50 frames/volume x 512 points/A-line and 51,200 A-lines/volume; 1024 A-lines/frame x 50 frames/volume x 512 points/A-line) were acquired of a 0.8 x 0.8 x 2.0 mm^3 section of the lateral compound eye of the horseshoe crab *in vivo*. Updates rates of 150, 75 and 40 frames/second were achieved with GPU computation respectively. Representative frames of the recorded videos show cross sectional images (left) and *en face* images (right) of a

few ommatidia within the lateral compound eye (Figure 2.8). *En face* depths of 380 μm (Figure 2.8 a,b) and 450 μm (Figure 2.8 c,d) are used for visualization in the *en face* image display. In all cases, every frame of data acquired by the OCT system running at full speed was processed for intensity and displayed to the screen.

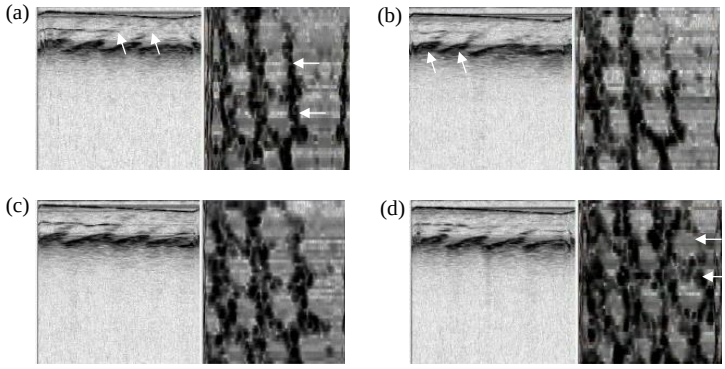

Figure 2.8: Representative frames from the video recordings demonstrating GPU-accelerated OCT imaging of the horseshoe crab eye. (a) 12,800 A-lines/volume: cross section and *en face* image 380 μm below the tissue surface (Media 1) (b) 25,600 A-lines/volume: cross section and *en face* image 380 μm below the tissue surface (Media 2) (c) 51,200 A-lines/volume: cross section and *en face* image 380 μm below the tissue surface (Media 3) (d) 25,600 A-lines/volume: cross section and *en face* image 450 μm below the tissue surface (Media 4). The arrows in the cross-sectional image of (a) point to the walls of crystal cones. The arrows in the *en face* images of (a) and (d) point to hexagonal ommatidia. Arrows in the cross-sectional image of (b) show membrane fenestrate at the end of the ommatidia.

Demonstration of GPU-accelerated OCT and PS-OCT imaging was done by volumetric imaging (12,800 A-lines/volume; 256 A-lines/frame x 50 frames/volume x 512 points/A-line) of the progression of thermal damage in a 1.3 x 1.3 x 2 mm^3 section of chicken muscle tissue. An update rate of 85 frames/second was achieved with GPU computation and allows the visualization of the change in birefringence that accompanies the progression of the thermal injury. The sample was continuously heated at one corner by a soldering iron at 720 F. Representative frames from the video depict the loss of birefringence (propagation of black color) in the cross-sectional image (Figure 2.9,

bottom left) and the *en face* image (Figure 2.9, top right) as the thermal damage progresses from the site of heat application (Figure 2.9). Denaturation of the collagen fibers that comprise muscle tissue occurs at high temperatures and accounts for the loss of birefringence seen in the video recording.

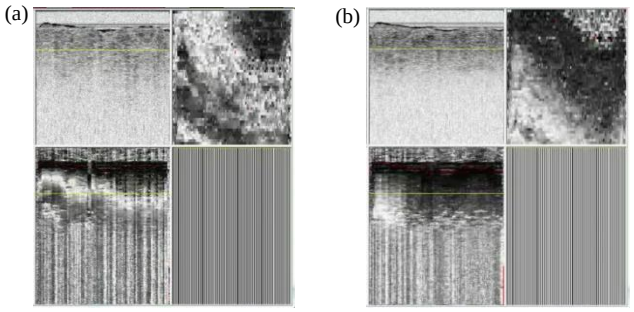

Figure 2.9: Representative frames from the video recordings demonstrating GPU-accelerated OCT and PS-OCT imaging of the progression of thermal damage in chicken muscle tissue (Media 5). *Top Left.* OCT cross-sectional image. *Bottom Left.* PS-OCT cross-sectional image. *Top Right.* PS-OCT *en face* image. *Bottom Right.* Unused view. (a) Screen capture of the GUI at the start of heat application. (b) Screen capture of the GUI after thermal damage had propagated to the surrounding tissue. The yellow line indicates the depth at which the *en face* image is reconstructed.

Demonstration of GPU-accelerated OCT and Doppler OCT imaging was done by volumetric imaging (102,800 A-lines/volume; 1028 A-lines/frame x 100 frames/volume x 512 points/A-line) of the flow of a diluted intralipid solution through a 1.8 x 1.8 x 2 mm^3 section of a microfluidic device. An update rate of 20 frames/second was achieved with GPU computation. The microfluidic device was constructed using a polydimethylsiloxane (PDMS) substrate with a 600 μm diameter channel etched into it. The PDMS substrate was bound to a 1.1 mm thick microscope glass slide. Tubes connecting the inlet and outlets were inserted and used to direct flow from a syringe using a syringe pump into a waste dish. The device was imaged such that the glass slide faced the final lens of the sample arm of the OCT system. A representative frame from

the video recording shows the structural image (Figure 2.10, top left), phase-variance processed flow image (Figure 2.10, bottom right) and *en face* phase variance processed flow image (Figure 2.10, top right) of the fluid flow through the microfluidic device (Figure 2.10). Arrows indicate the top and bottom surfaces of the glass slide. The cross-sectional flow image shows black and white rings in the channel region indicating areas of phase wrapping occurring due to a high volumetric flow rate. Additionally, the flow profile depicts two distinct regions within the channel, consistent with the presence of turbulent flow and the observations made by Bonesi et al. [46].

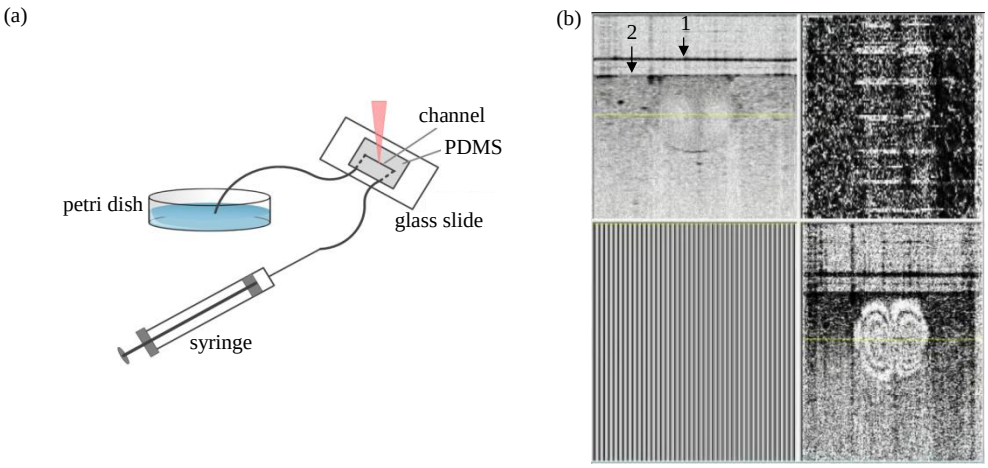

Figure 2.10: Representative frame from the video recordings demonstrating GPU-accelerated OCT and Doppler OCT imaging of the flow of a diluted intralipid solution through a microfluidic device (Media 6). *Top Left.* OCT cross-sectional image. *Bottom Left.* Unused view. *Top Right.* Doppler OCT *en face* image. *Bottom Right.* Doppler OCT cross-sectional image. (a) Schematic of the experimental setup. (b) Screen capture of the GUI during intralipid flow through the microfluidic device. The yellow line indicates the depth at which the *en face* image is reconstructed. Arrow 1 in (b) points to the top surface of the glass slide and arrow 2 in (b) points to the bottom surface of the glass slide that the PDMS microfluidic device is attached to.

Finally, demonstration of full GPU-accelerated multi-functional OCT imaging (OCT, PS-OCT and Doppler OCT) is done via *in vivo* volumetric imaging (409,600 A-lines/volume; 2048 A-lines/frame x 200 frames/volume x 512 points/A-line) of a 2 x 2 x

2 mm^3 section of a mouse brain. An update rate of 10 frames/second was achieved with GPU computation. The skull of an anesthetized mouse was thinned to reduce light scattering from the skull and allow for deeper penetration of the OCT light into the brain tissue. Images of the structure (Figure 2.11, top left), polarization properties (Figure 2.11, bottom left), blood flow (Figure 2.11, top right) and vascular network (Figure 2.11, *en face*, bottom right) can be seen in a representative frame from the video recording (Figure 2.11). The yellow line in the cross-sectional image views indicates at which depth the *en face* image is being displayed. White arrows indicate areas of blood flow and the presence of vascular networks in the flow and *en face* flow images respectively. The black arrow in the structural image indicates a region of higher scattering consistent with the corpus callosum. The PS-OCT image shows that the cortex of the mouse is weakly birefringent due to the slow transition of color map values from black to gray.

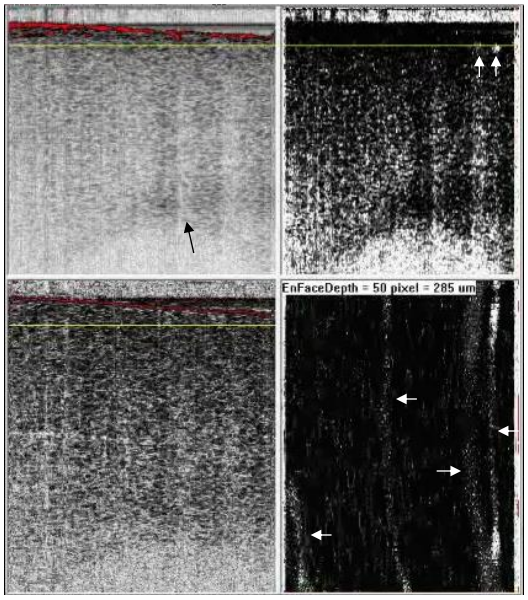

Figure 2.11: Representative frame from the video recording demonstrating GPU-accelerated multi-functional OCT imaging of a mouse brain *in vivo* (Media 7). *Top Left.* OCT cross-sectional image. *Bottom Left.* PS-OCT cross-sectional image. *Top Right.* Doppler OCT cross-sectional image. *Bottom Right.* Doppler OCT *en face* image. The arrow in the OCT cross-sectional image points to the corpus callosum. The yellow line indicates the depth at which the *en face* image is reconstructed. The arrows in the Doppler OCT cross-sectional image points to two blood vessels. The arrows in the Doppler OCT *en face* image point to blood vessels seen at a depth of 285 μm below the surface.

Section 2.4.2: Three-dimensional GPU-accelerated OCT processing

The performance enhancement of three-dimensional multi-functional OCT imaging using CUDA-based processing and OpenGL visualization is demonstrated by volumetric imaging of the human finger nail fold, the progression of thermal damage due to localized heating of chicken muscle tissue and the femoral arteries and veins of a mouse *in vivo*. This is visualized with video recordings of the volumetric view of the GUI of the software application during acquisition of images from the aforementioned samples.

Demonstration of the volumetric visualization of simultaneous OCT and PS-OCT data is done by volumetric imaging (256 A-lines/frames x 64 frames/volume x 256 points/A-line) of a 2.4 x 2.4 x 1 mm^3 section of a human finger nail fold *in vivo*. Representative frames from the video recordings show the structural (Figure 2.12, left images) and birefringent (Figure 2.12, right images) volumetric images of the section of the finger nail fold from two different perspectives (Figure 2.12). The perspective of the camera is controlled by the user via interaction with the GUI. Mouse clicks and drags are translated into distances that are fed into the model-view matrix and updated between successive volumetric image renderings.

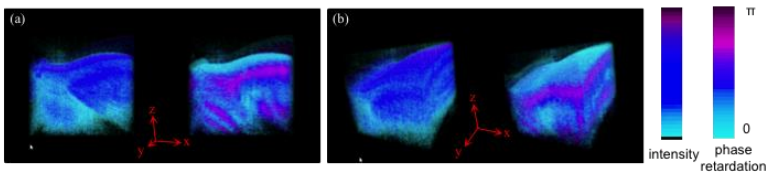

Figure 2.12: Representative frame from the video recording demonstrating volumetric OCT and PS-OCT imaging of a human finger nail fold *in vivo*. Images (a) and (b) are two screen captures of the volumetric view of the software with differing perspectives.

Demonstration of the utility of volumetric visualization to monitor injury progression in biological tissue is done by repeated volumetric imaging (256 A-lines/frame x 64 frames/volume x 256 points/A-line; 512 A-lines/frame x 128 frames/volume x 512 points/A-line) of the progression of thermal injury in 1.2 x 1.2 x 1 mm^3 and 1.2 x 1.2 x 2 mm^3 sections of chicken muscle tissue respectively. The sample was continuously heated at one corner by a soldering iron at 720 F. Representative frames from the video depict the loss of birefringence (propagation of cyan color and loss

of pink color stripes) in the volumetric images as the thermal damage progresses from the site of heat application (Figure 2.13).

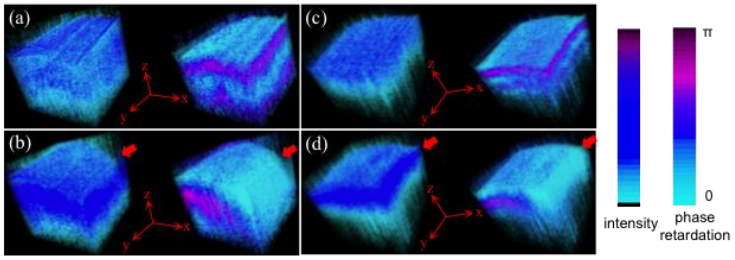

Figure 2.13: Representative frame from the video recording demonstrating volumetric OCT and PS-OCT imaging of the progression of thermal damage in chicken muscle tissue. *Left Images.* OCT volumetric images. *Right Images.* PS-OCT volumetric images. Images (a) and (b) are screen captures of the volumetric view of the software at two different time points during the progression of thermal damage (256 A-lines/frame x 64 frames/volume x 256 points/A-line). Images (c) and (d) are similar screen captures of a differently sized volume (512 A-lines/frame x 128 frames/volume x 512 points/A-line).

Demonstration of the volumetric visualization of full multi-functional OCT is done by repeated volumetric imaging (256 A-lines/frame x 64 frames/volume x 256 points/A-line; 512 A-lines/frame x 128 frames/volume x 512 points/A-line) of 0.8 x 0.8 x 1 mm^3 and 1.2 x 1.2 x 2 mm^3 exposed sections of the femoral area of the mouse leg *in vivo*. Within the section of images tissue lie the femoral artery and vein surrounded by connective tissue. Representative frames from the video recordings show the highly pulsatile nature of arterial flow and weakly pulsatile nature of venous flow assessed with phase-variance-based Doppler OCT (Figure 2.14). The Doppler OCT volumetric images (Figure 2.14, right images) were superimposed with the OCT (Figure 2.14, left images) and PS-OCT (Figure 2.14, middle images) volumetric images for simultaneous visualization of structural and functional information. The larger Doppler OCT

volumetric images show a train of pulses due to the longer rendering times of larger volumetric images (0.5 volumes/second as compared to 2 volumes/second).

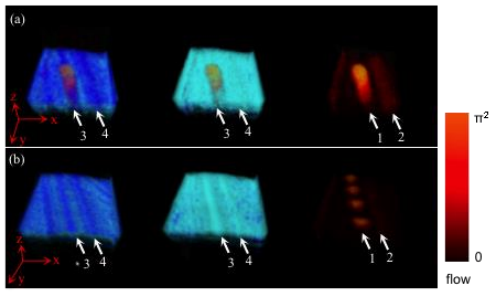

Figure 2.14: Representative frame from the video recording demonstrating volumetric multi-functional OCT imaging of the femoral area of a mouse leg *in vivo*. *Left Images.* Overlaid OCT and Doppler OCT volumetric images. *Middle Images.* Overlaid PS-OCT and Doppler OCT volumetric images. *Right Images.* Doppler OCT volumetric images. (a) Screen capture of the volumetric view of the software showing a single pulse of blood flow in an artery (256 A-lines/frame x 64 frames/volume x 256 points/A-line). (b) Similar screen capture of the blood vessel showing 4 pulses (512 A-lines/frame x 128 frames/volume x 512 points/A-line).

Section 2.5: Discussion

The combination of NVIDIA GPUs and CUDA-based multi-functional SD-OCT data processing algorithms developed in house enabled our SD-OCT to perform high-speed multifunctional OCT imaging. The first generation of our GPU-accelerated data processing algorithms together with the NVIDIA Tesla C1060 resulted in a 6x speedup in processing speeds compared with its CPU counterpart. Demonstrations of the speedup included structural OCT imaging of the horseshoe crab lateral compound eye, PS-OCT imaging of the loss of birefringence in chicken muscle as a result of thermal damage, D-OCT imaging of intralipid flow through the micro-channel of a microfluidic device and *in vivo* multi-functional OCT imaging of the mouse cortex. These demonstrations highlight the ability of the system to rapidly assess biological samples as well as monitor

fast dynamic biological phenomena. However, the processing speed of multi-functional OCT data still exceeded that of the fastest acquisition of our line scan cameras which prevented us from fully realizing real-time multi-functional OCT imaging.

Our second generation of GPU-accelerated OCT data processing algorithms combined with the NVIDIA Tesla K20 resulted in an overall speed up of 100x over CPU-based processing methods. On the hardware side, the Tesla K20 GPU uses the newest Kepler architecture and has 2496 cores that allow for massively parallel processing. On the software side, we optimized the run-time of our algorithms by reducing memory usage by the kernels, and used zero-copy memory to remove the host-device copy times. Zero-copy memory, or pinned memory, uses a universal address that is accessible by the host and device and eliminates the need for an explicit data transfer to device memory. The 100x speed up obtained with these improvements reduced our processing times such that our multi-functional OCT system can image in real-time, limited only by the speed of the line scan cameras. Additionally, these processing times are fast enough to allow for an upgrade to faster line scan cameras and allow for additional computation to be performed while still staying below the data acquisition time.

We used the time gap between GPU-accelerated processing and data acquisition to implement volume rendering computation into our software. Demonstrations of the volume rendering capabilities of the software included volumetric OCT and PS-OCT imaging of the human finger nail fold, volumetric OCT and PS-OCT of the progression of thermal damage in chicken muscle tissue and *in vivo* volumetric MF-OCT imaging of the femoral area of the mouse leg. These demonstrations highlight the ability of the

system to structurally and functionally assess biological samples and monitor dynamic biological phenomena in three dimensions. Currently, both the 2D and 3D GPU-accelerated data processing occurs on a single GPU installed into our workstation which results in the full 3D processing speed exceeding the 3D data acquisition speed. Improvement in the 3D processing speed can be obtained by performing the volume rendering computation on a second GPU in parallel with the 2D OCT data processing of the first GPU. Reconfiguration of the internal data stream of the software and implementation of the CUDA streams and device-device data copy features in the CUDA API make this possible and should result in our 3D computation speeds to be faster than the 3D acquisition speeds of the line scan cameras.

Section 2.6: Conclusions

In summary, this chapter described the development of a GPU-accelerated MF-SD-OCT imaging system capable of high-speed 2D and 3D imaging of biological samples. The total speed up obtained with GPU-accelerated processing algorithms reduced our 2D processing times such that our MF-SD-OCT system can image is limited only by the speed of the line scan cameras. Demonstrations of the GPU-accelerated 2D MF-SD-OCT processing included structural OCT imaging of the horseshoe crab eye, PS-OCT imaging of the progression of thermal damage in chicken muscle tissue, Doppler OCT imaging of fluid flow through a microfluidic device and MF-OCT of the mouse cortex *in vivo*. Demonstrations of the GPU-accelerated 3D MF-SD-OCT processing and visualization included volumetric OCT and PS-OCT imaging of the human finger nail

fold, volumetric OCT and PS-OCT of the progression of thermal damage in chicken muscle tissue and volumetric MF-OCT of the femoral area of a mouse *in vivo*. This system enables rapid structural and functional assessment of biological samples and monitoring of fast dynamic biological phenomena across all three spatial dimensions. Continued improvement of the computing configuration and software will enable high-speed real-time volumetric MF-SD-OCT imaging of biological tissue samples. Additionally, this will provide computing time that can be used for high-speed real-time imaging of cellular samples with newly developed processing work flows that will be discussed in Chapter 4.

Chapter 3: Optical characterization of biological tissue using spectral-domain optical coherence tomography and polarization-sensitive optical coherence tomography

This chapter describes the development of algorithms for optical characterization of biological tissue from OCT and PS-OCT images. The chapter is organized into three sections: an introduction to tissue optics and absorption, scattering, diattenuation and birefringence phenomena (Section 3.1), a section on the development of algorithms to characterize absorption and scattering and nerve structural features from OCT images (Section 3.2) and a section on the development of algorithms to characterize birefringence and nerve structural features from PS-OCT images (Section 3.2). These algorithms were used in a study focused on characterizing optical properties of *ex vivo* nerve and *in vivo* nerve and muscle tissue from a rat [47].

Structural OCT images are generated by spatially resolving backscattered light from biological tissues. The magnitude of the backscattered light is directly related to the interactions of light with the materials that comprise the tissue. These interactions are non-specific light-tissue interactions and occur across all biological materials and all wavelengths of light. This makes it difficult to distinguish features within biological tissues and distinguish biological tissues from one another on the basis of spatially-resolved backscattered light alone (Figure 3.1).

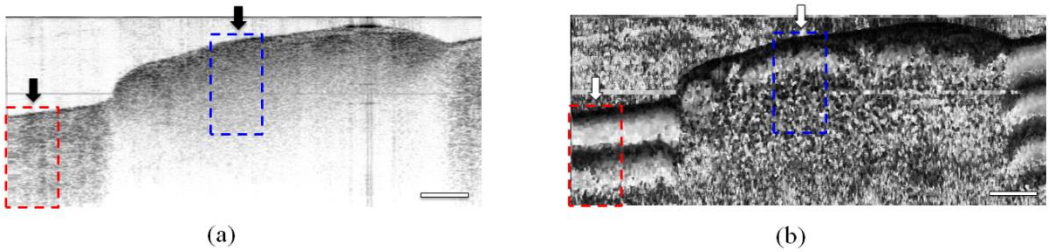

Figure 3.1: *In vivo* OCT (a) and PS-OCT (b) images of the rat sciatic nerve surrounded by muscle tissue. Red boxes indicate regions of muscle tissue and blue boxes indicate regions of nerve tissue.

PS-OCT images are generated by spatially resolving the birefringence of biological tissues. Birefringence is the result of specific interactions between light and a subset of organized biological. This makes PS-OCT imaging a high-contrast extension of OCT and a useful tool for distinguishing biological tissues using intrinsic contrast. The light-tissue interactions that underlie OCT and PS-OCT images and the measurement methods developed in this chapter are discussed below.

Section 3.1: Introduction to light-tissue interactions

Consider a thin, single-layer biological tissue sample in air illuminated by a monochromatic unpolarized light source I_o. In simplest terms, photons emitted from this source can be spatiotemporally characterized by an amplitude *A* and phase ϕ:

$$E(z,t) = A\exp\left(-i\left(kz-\omega t\right)\right) = A\exp\left(-i\phi\right) \tag{3.1}$$

Light interacts with the biological sample in a variety of different ways depending on the composition of the sample (Figure 3.2). As the photons from the light source hit the tissue sample, they experience a refractive index mismatch between the air and the tissue sample resulting in two possible outcomes for the photons: (1) they undergo specular

reflection and simply bounce off and away from the tissue surface or (2) they enter the tissue and undergo additional interactions with the tissue sample. As photons begin to propagate within the tissue, they undergo two main interactive processes: absorption and scattering. Absorption is the extinction of the energy of a photon, terminating its propagation. Scattering is the change in propagation direction of a photon. The scattering phenomenon is further classified into elastic and inelastic regimes based on the energy of the scattered photon relative to the energy of the incident photon. It is also classified into Mie and Rayleigh scattering regimes based on the relative ratio between the size of the scattering particle and the wavelength of the incident photon. Mie scattering is the dominant form of scattering by biological tissues and is the basis for measurements made with SD-OCT. Photons can undergo multiple scattering events while propagating through biological tissue and can exit the tissue sample in multiple ways. Diffuse reflectance is the exit of photons from the entry surface after undergoing at least one scattering event while propagating through the tissue. Transmission is the propagation of photons through the full thickness of the tissue sample. It is important to note that all of these processes are wavelength-dependent.

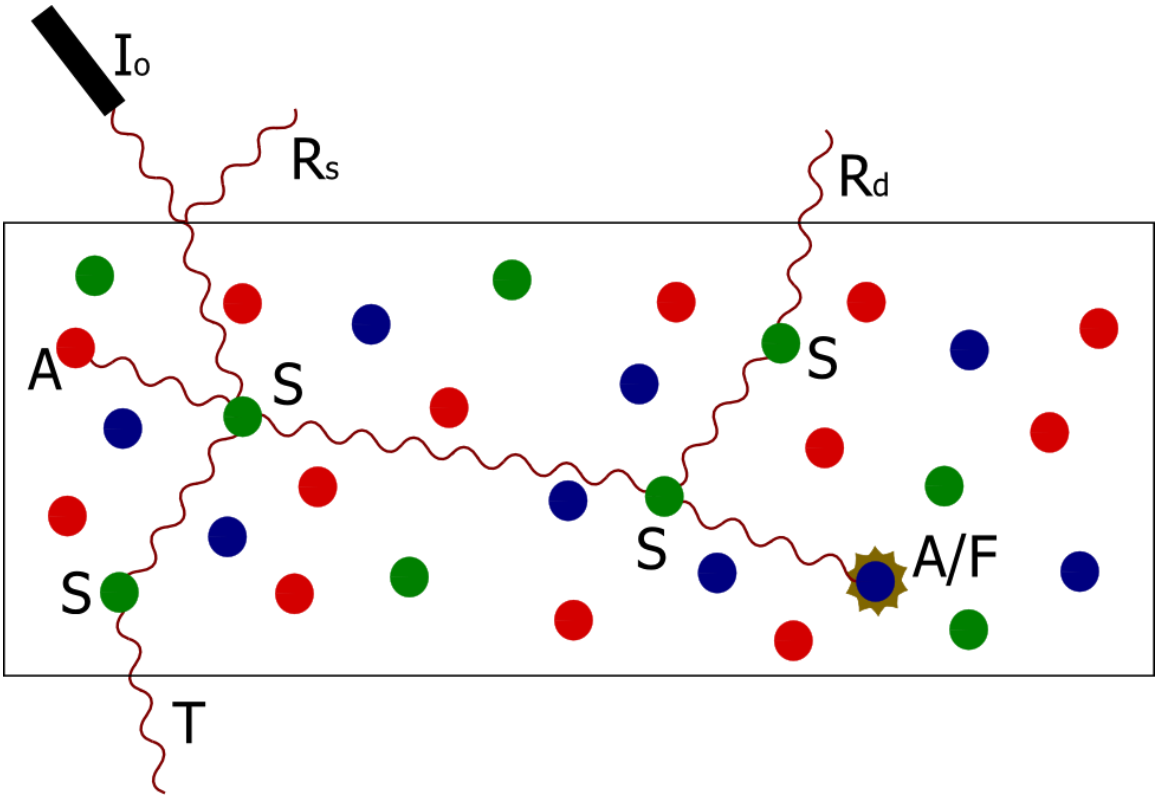

Figure 3.2: Diagram of the possible interactions photons can undergo within a biological tissue sample. I_o: source intensity, R_s: specular reflectance, S: scattering event, A: absorption event, T: transmission, A/F: absorption and fluorescence, R_d: diffuse reflectance. Green dots: scattering particles, Red dots: absorbing particles, Blue dots: fluorescent particles.

Absorption and scattering are two quantitates that are used to characterize the light attenuation properties of the tissue. Light propagating through a biological tissue sample will undergo an increasing number of absorption and scattering events as the distance it travels increases. This results in light distributions that decay exponentially as a function of distance traveled and can be written as:

$$I_{x,a} = I_o exp\left(-\mu_a x\right) \tag{3.2}$$

$$I_{x,s} = I_o exp\left(-\mu_s x\right) \tag{3.3}$$

where I_x is the light distribution as a result of absorption or scattering processes, I_o is the incident light intensity, μ_a is the absorption coefficient, μ_s is the scattering coefficient and *x* is the distance traveled by the light. The total attenuation of the light by biological tissue is the sum of the contribution of absorption and scattering processes and is given by:

$$I_x = exp\left(-\mu_t x\right) \tag{3.4}$$

where $\mu_t = \mu_a + \mu_s$. The absorption and scattering events that underlie light attenuation are governed by the composition of the tissue. This allows the use of light attenuation as a means of distinguishing different biological tissues.

If the photons emitted from the light source are polarized, these photons can undergo two additional polarization-dependent processes as they propagate through biological tissue. As mentioned previously, the polarization state of light can be exactly characterized by the amplitude ratio and phase difference between the orthogonal electric field components. A change in the amplitude ratio of orthogonal polarization states is called diattenuation (1.14) and a change in the relative phase difference between two orthogonal polarization states is called birefringence (1.15). Tissues exhibiting these polarization-dependent phenomena have an optical axis associated with them. The optical axis of the tissue for a given effect is the direction a light ray can travel and propagate unaffected (i.e. the optical axis of a material for diattenuation is the direction in which a light ray can travel and not experience any diattenuation. This is true for birefringence as well). Birefringence is the dominant polarization-dependent property exhibited by biological tissue. As with total light attenuation, birefringence is also dependent on the

composition of the underlying tissue. Well-organized and cylindrical structures induce birefringence in the light that interacts with it. Biological materials like myelin, collagen and myofibrils, as well as their organization with tissue, make nerve and muscle tissues birefringent and the absence of these materials from fat tissue makes it a non-birefringent tissue. This allows the use of birefringence for distinguishing biological tissues with additional contrast compared with light attenuation alone given that a small subset of tissues are composed of well-organized birefringent biological materials.

Section 3.2: Optical characterization of biological tissue using OCT and PS-OCT

Methods for optical characterization of biological tissue from OCT and PS-OCT data were developed and verified by *in vivo* OCT and PS-OCT imaging of the sciatic nerve of 18 Sprague-Dawley rats. These rats are widely used in nerve injury and recovery studies [48,49,50]. This animal model allows for the manipulation of a peripheral nerve of similar caliber and size to the human digital nerve and allows for objective assessment of motor function following injury. The Massachusetts General Hospital Institutional Subcommittee on Research Animal Care (SRAC) approved all procedures described. Anesthesia was administered via an intraperitoneal injection of pentobarbital sodium (50 mg⁄kg, Abbott Laboratories Chicago, IL). This was followed by surgical exposure of the right sciatic nerve via a dorsolateral muscle splitting incision and *in vivo* OCT and PS-OCT imaging. The OCT system used for imaging is fully described in the literature [35]. Briefly, the OCT system is a spectral-domain OCT system with a center wavelength of 1320 nm and a FWHM of 68 nm (Figure 3.3). Light sent into the interferometer was first

sent through an electro-optic polarization modulator to allow switching between orthogonal polarization states. A 90/10 splitter split the light into sample and reference arms of the interferometer respectively. Light returning from both arms passed back through the system and was sent to a polarization-sensitive spectrometer. In the spectrometer, light was dispersed by a diffraction grating (1100 lines per mm) and split by a polarization beam splitter onto two 512-element InGaAs line scan cameras with a maximum line speed of 18.5 kHz. The axial resolution was 11 microns up to a depth of 1.0 mm, in good agreement with calculations based on the light source specification, and increased to 14 microns at a depth of 1.8 mm. The focused spot size of the scanning beam was 22.4 μm in diameter. The imaging depth was found to be 2.0 mm in air with a sensitivity drop-off of 8 dB over that range. A multi-threaded software application written in Microsoft Visual C++ running on a dual-processor computer managed data acquisition and updated displays for spectrum, intensity, polarization, and flow, as well as saved data to the hard drive for post-processing of images.

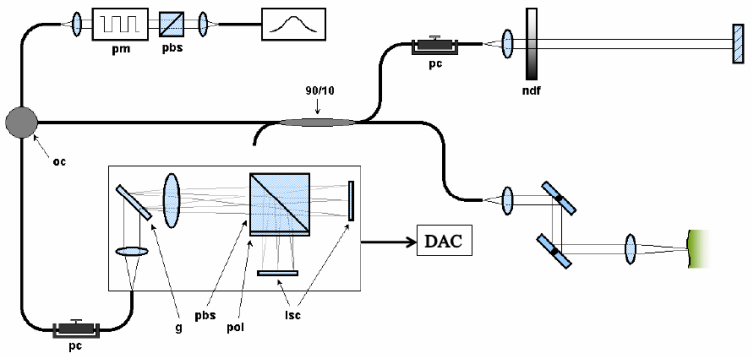

Figure 3.3: System diagram of the multi-functional spectral-domain OCT imaging system centered at 1300 nm. pbs: polarizing beam splitter, pm: polarization modulator, oc: optical circulator, 90/10: fiber beam splitter, pc: polarization controller, ndf: neutral density filter, g: grating, pol: polarizer, lsc: line scan camera, DAC: data acquisition computer.

Raster scanning of the sample arm was performed with the fast axis perpendicular to the long axis of all nerves. Volumetric intensity images were comprised of 2048 A-lines/frame and 200 frames/volume, spanning a 5 x 2 x 5 mm section of the tissue. Volumetric PS-OCT images of the same section were simultaneously generated. Acquisition of the volumetric images required 22 seconds at an A-line rate of 18,500 Hz. Each image was processed individually using Matlab® 2009b in a graphics-processing unit (GPU)-enabled multicore processor computer. Image processing techniques similar to an earlier study [51] were followed for intensity and polarization processing. Volumetric reconstructions from these cross-sectional images were done using a 3D visualization software package (Amira, Visage Imaging Inc.).

Section 3.2.1: Epineurium thickness measurement

The epineurium is a layer of connective tissues that surrounds peripheral nerves. One of the objectives of this work was to measure the thickness of this layer and precisely define its boundaries to help identify the positions of axons and the mesoneurium within the epineurium. To do this, the middle 50% of the nerve in both OCT and PS-OCT images was used for quantitative analysis to minimize artifact from surrounding connective tissue. The curvature of the nerve surface was flattened such that pixels in each depth profile represent the same physical depth. These adjusted depth profiles were averaged to get an average depth-resolved intensity and phase retardance for OCT and PS-OCT images respectively. Depth-resolved intensity data was converted to a logarithmic scale for data fitting. A linear fit of the curve corresponding to the axonal

region of the nerve was performed and extrapolated over the entire depth range. We assume that the axonal region of the tissue will have unique and uniform optical properties that differ from those of the epineurium. We then calculate the absolute value of the residuals between the linear fit and actual curve (Figure 3.4). A threshold value corresponding to the mean plus two standard deviations of the residuals from the fit of the axonal region is shown (dotted line) to help determine the epineurium-axonal region boundary. We considered the intersection of the residuals curve and the threshold line as the posterior boundary of the epineurium and the nerve tissue and air interface as the anterior boundary of the epineurium. These locations allow us to calculate the thickness of the epineurium from the *ex vivo* OCT images.

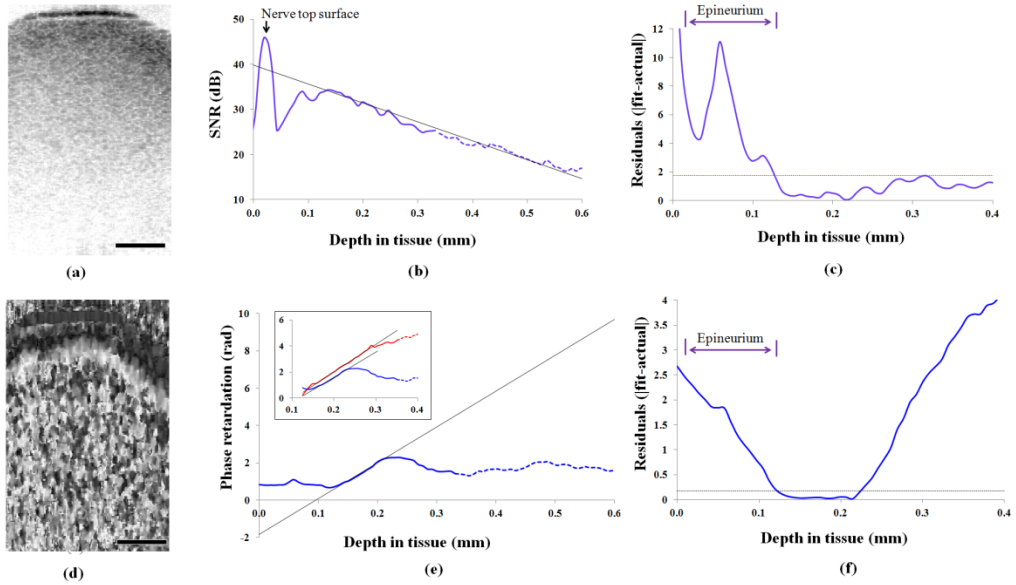

Figure 3.4: Diagram of the procedure used to measure epineurial thickness of peripheral nerves from OCT and PS-OCT images. (a) OCT cross-sectional image of an *ex vivo* rat sciatic nerve, (b) Average SNR vs. tissue depth plot used to determine how and where to fit the interior axonal region of the nerve, (c) Residual difference between the fit and experimental data plotted against tissue depth to determine where significant deviation from the fit occurs, (d) PS-OCT cross-sectional image of an *ex vivo* rat sciatic nerve (e) Average phase retardance vs. tissue depth plot used to determine how and where to fit the interior axonal region of the nerve, (f) Residual difference between the fit and experimental data plotted against tissue depth to determine where significant deviation from the fit occurs. Dotted lines indicate regions in which the SNR dropped below 25 dB. Scale bars: 200 µm.

To measure the epineurium thickness from PS-OCT images, we began with the averaged depth-resolve phase retardance profile from the middle 50% of the nerve. In a similar fashion, a linear fit of the curve correspond to the axonal region was performed and extrapolated over the entire depth range. We then calculate the absolute value of the residuals between the linear fit and actual curve (Figure 3.4). A threshold value corresponding to the mean plus two standard deviations of the residuals from the fit of the axonal region is shown (dotted line) to help determine the epineurium-axonal region boundary. We considered the intersections of the residuals curve and the threshold line as the anterior and posterior boundaries of the epineurium. These locations allow us to

calculate the thickness of the epineurium from the *ex vivo* PS-OCT images. However, due to the Stokes method of analysis performed, the average depth-resolved phase retardance profile suffers from phase wrapping artifacts [35]. To verify the homogeneity of optical properties in this region and ensure that phase wrapping is not misleading our epineurium thickness measurements, we performed a Jones matrix analysis of the PS-OCT data. The Stokes method of analysis suffers from phase wrapping while the Jones matrix method does not. We observed a similar slope in the Jones matrix method up to a depth of 0.3 mm as in the Stokes method (Figure 3.4 inset). Beyond 0.3 mm, the SNR became too low to extract reliable phase information. We found that the minimum SNR required for extracting reliable phase information is 25 dB. Broken lines in Figure 3.4 indicate depths within the OCT image at which the SNR drops below 25 dB.

Epineurium thickness measurements from OCT and PS-OCT images are summarized in Figure 3.5. Average epineurium thickness from OCT images was found to be 0.133 ± 0.014 mm (mean ± standard deviation). In comparison, the average epineurium thickness from PS-OCT images was found to be 0.129 ± 0.009 mm. The analysis was repeated for nerves under increasing longitudinal tensile stress (nerve lengths increasing up to 20% of its original length) and show no significant difference in epineurium thickness (Figure 3.5). The measured values agree well with previously reported measures of rat sciatic-nerve epineurium thickness [52,53].

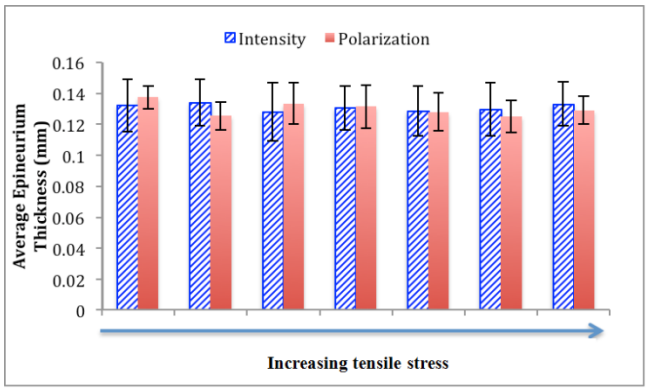

Figure 3.5: Summary of epineurial thickness measurements from OCT and PS-OCT images as a function of tensile stress on the nerve. Blue hashed bars indicate thickness measurements from OCT images and red bars indicate thickness measurements from PS-OCT images. Error bars represent 1 standard deviation away from the mean.

Section 3.2.2: Bands of Fontana analysis

The Bands of Fontana are a well-known optical phenomena that occurs due to differential light scattering from periperhal nerve microstructures [54,55,57,58]. The undulating nature of small nerve fibers inside the bundle cause an appearance of dark and light stripes on the surface of the fascicule. Their visibility depends both on the degree to which a nerve is under tension and on the angle of illumination [54,55,57,58]. Although an oblique illumination angle is more suitable to see the bands, the normally incident optical beam used in OCT still provides sufficient visualization of the bands in both OCT and PS-OCT volumetric images. These bands are more easily seen in static volumetric OCT and PS-OCT images (Figure 3.6) but are more easily seen by virtually slicing through the volumetric images with 3D reconstruction software.

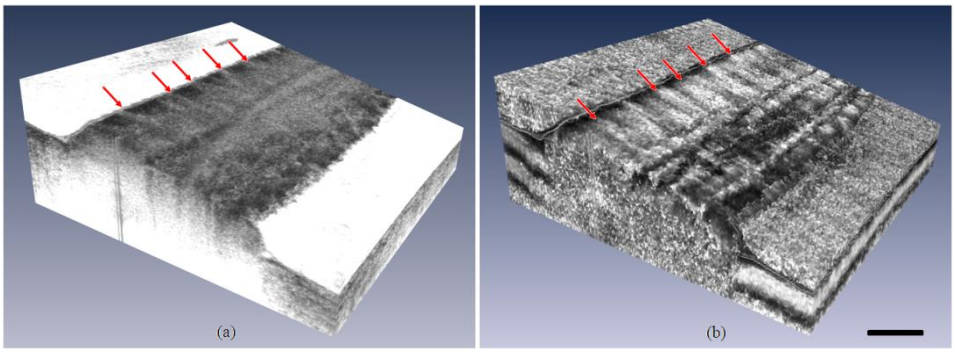

Figure 3.6: 3D reconstructions of volumetric OCT and PS-OCT image data of an *in vivo* section of the rat sciatic nerve surrounded by muscle. (a) OCT 3D reconstruction, (b) PS-OCT 3D reconstruction. Red arrows indicate the presence of the Bands of Fontana visible in both reconstructions. Scale bar: 1 mm.

To quantitatively analyze these bands, we analyzed the intensity trend along the long axis of the nerve from *ex vivo* intensity images. We chose a depth of ~300 μm for the analysis because the bands were the most visible at that depth. For each B-scan, the intensity at that depth in multiple depth profiles were averaged to obtain a single intensity value. The trends can be seen in Figure 3.7b and Figure 3.7d for an unstretched and stretched nerve respectively. It can be seen that the intensity plot corresponds well with the appearance of the Bands of Fontana in the OCT images (Figure 3.7a,c). Previous studies have reported decreased visibility of the Bands of Fontana when a nerve is stretched due to the altered undulation of the nerve microstructure within the fascicule [55,57]. We observed a similar phenomena in this study. A stretched nerve exhibited a smaller number of visible bands over the length of the nerve compared to the unstretched nerve (Figure 3.7). We quantified the spatial frequency of visible bands for stretched and unstretched nerves by counting the number of bands in a given nerve segment and dividing it by the total length of the segment. As expected, there is a higher spatial frequency of bands for the unstretched nerve (2.5 bands⁄mm) compared to the stretched

nerve (1 band/mm). The average distance between adjacent bands in the unstretched nerve is between 300 and 400 μm which agree well with previous reports [55].

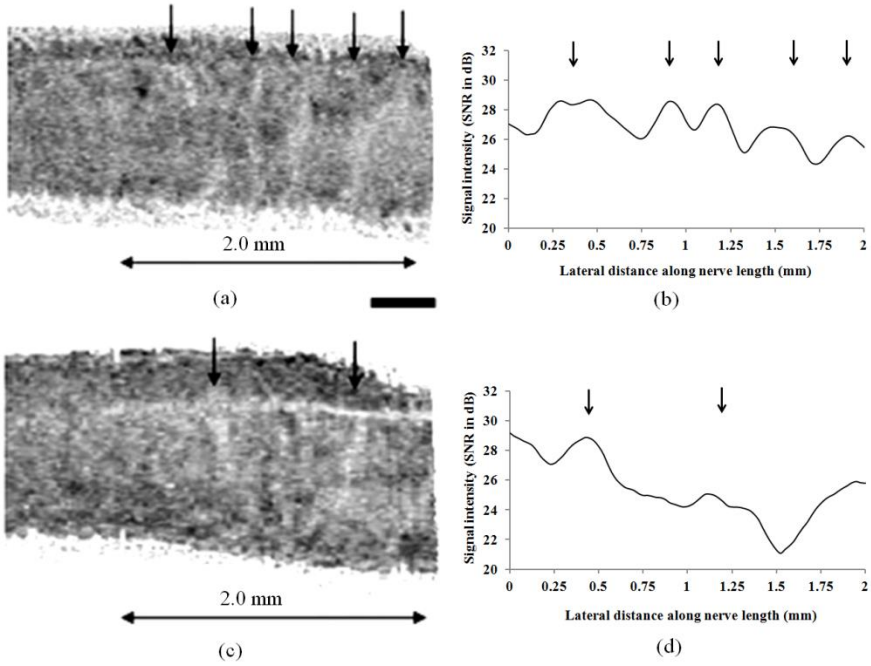

Figure 3.7: Quantitative analysis of the frequency of the Bands of Fontana for un-stretched and stretched nerves. (a,c) *en face* OCT images of the rat sciatic nerve at depths of 300 μm for un-stretched and stretched nerves respectively. (b,d) Average intensity plots along the long axis of the un-stretched and stretched nerves respectively. Arrows indicates the presence of visible bands. Scale bar: 400 μm.

Section 3.2.3: Stretch-induced birefringence changes

Additionally, we wanted to investigate whether any changes in birefringence occur due to the stretching of a nerve. A 2 cm nerve segment was progressively stretched to a final length of 2.4 cm (a 20% increase in length). At five different amounts of stretch, birefringence measurements from multiple PS-OCT B-scans along the nerve length were taken and averaged to obtain a representative measurement. The results demonstrate that

the average birefringence throughout the volume of the nerve does not change appreciably with stretch (Figure 3.8).

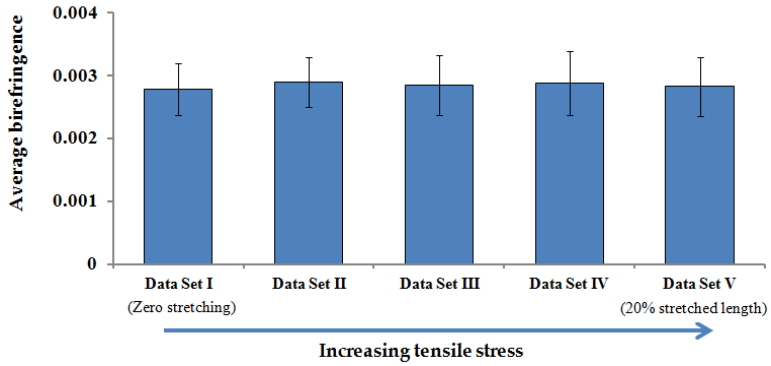

Figure 3.8: Summary of average birefringence measurements of nerves under increasing amounts of tensile stress. Error bars represent one standard deviation from the mean.

Section 3.2.4: Optical property measurements

The classification of tissues via the attenuation coefficient is demonstrated by OCT imaging of the sciatic nerve of a rat *in vivo*. A representative OCT image of this area shows a segment of the sciatic nerve surrounded by muscle tissue (Figure 3.9a). The red and blue boxes indicate the regions used to calculate the attenuation coefficient of muscle and nerve tissue respectively. The attenuation coefficient was calculated by exponentially fitting the intensity drop-off averaged over the 200 A-lines that are encompassed in the boxed regions (Figure 3.9c,e). Specifically for nerve tissue, the analysis was restricted to the region within the epineurium to determine the attenuation coefficient of the myelinated axonal tissue in the nerve interior.

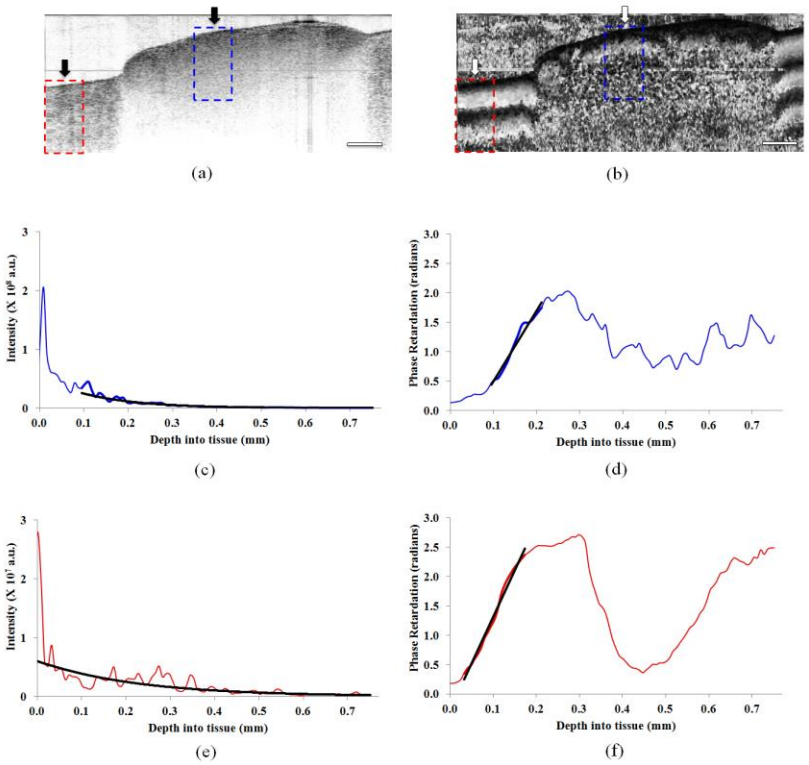

Figure 3.9: Procedure for measuring optical properties of nerve and muscle tissue from OCT and PS-OCT images. (a,b) *in vivo* OCT and PS-OCT images of the rat sciatic nerve surrounded by muscle respectively, (c,e) Average linear intensity vs. tissue depth plots to demonstrate the fitting regions for computing the attenuation coefficient of nerve and muscle tissue respectively, (d,f) Average phase retardance vs. tissue depth plots to demonstrate the fitting regions for computing the birefringence of nerve and muscle tissue respectively. Red and blue boxes indicate regions of nerve and muscle tissue used in optical property calculations respectively. Scale bars: 1 mm.

Multiple measurements made for each rat at 22 different cross-sections along the length of the sample give a total of 396 measurements of attenuation coefficient for nerve and muscle tissue (Figure 3.10). The distributions of attenuation coefficient demonstrate higher light attenuation by nerve tissue compared to muscle tissue which agrees well with previous studies [56]. The attenuation coefficient distributions for nerve tissue (9.08 ± 1.14 mm^{-1}) and muscle tissue (4.75 ± 1.27 mm^{-1}) are distinct and no significant overlap exists between them. A two-tailed Students T-test showed strong statistical differences

between the attenuation coefficient distributions of nerve and muscle tissue ($t = 14.14$, $p < 0.001$).

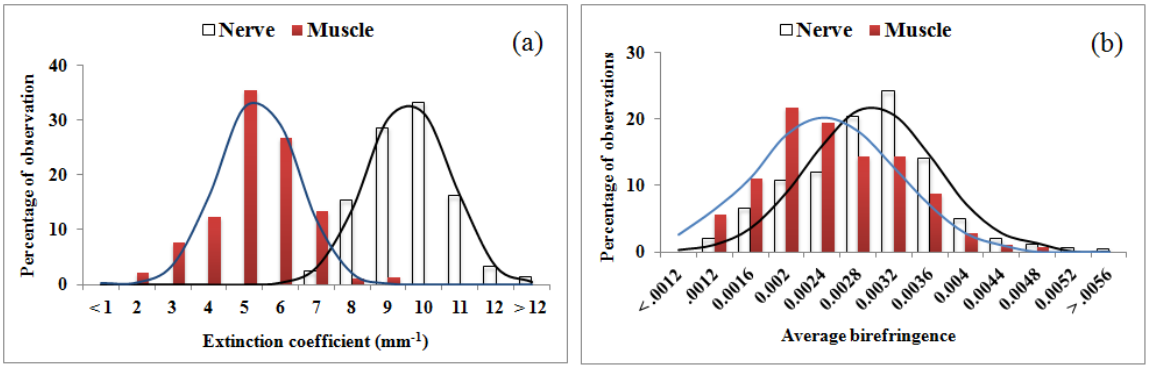

Figure 3.10: Distributions of attenuation coefficient and birefringence measurements of nerve and muscle tissue. (a) Attenuation coefficient distributions of nerve (white) and muscle (red) tissue, (b) Birefringence distributions of nerve (white) and muscle (red) tissue.

The classification of tissues via birefringence is demonstrated by PS-OCT imaging of the sciatic nerve of a rat *in vivo*. A representative PS-OCT image of this area shows a segment of the sciatic nerve surrounded by muscle tissue (Figure 3.9b). The red and blue boxes indicate the regions used to calculate the birefringence of muscle and nerve tissue respectively. The birefringence was calculated by extracting the slope of a linear fit of the phase retardation averaged over the 100 A-lines that are encompassed in the boxed regions and multiplying (Figure 3.9d,f). Half the number of A-lines is used to determine birefringence because PS-OCT images contain half the number of A-lines of OCT images. This ensures that the analysis is performed over the same physical region of tissue as the attenuation coefficient. Similarly, the analysis of birefringence of nerve tissue was restricted to the region within the epineurium to determine the birefringence of the myelinated axonal tissue in the nerve interior.

The number and locations of measurements of birefringence of nerve and muscle tissue exactly mirror the number and locations of attenuation coefficient measurements. (Figure 3.10). The distributions of birefringence demonstrate slightly higher birefringence by nerve tissue compared to muscle tissue. The birefringence distributions for nerve tissue (0.00306 ± 0.0007) and muscle tissue (0.00268 ± 0.0007) overlap significantly. A two-tailed Students T-test showed no statistical difference between the birefringence distributions of nerve and muscle tissue ($t = 1.45$, $p = 0.15$).

Section 3.3: Discussion

The goal of the work presented is to develop methods of obtaining biologically-useful measurements from OCT and PS-OCT image data that can be used to study nerve injury at a level inaccessible to any currently existing technology. This becomes especially important in assessing the extent of nerve damage when the nerve exhibits no external manifestations of the injury i.e. if the interior axonal structures are disrupted but the outer connective tissue layer is intact. OCT is well-suited for this task given its micron level spatial resolution and millimeter level penetration depth. Quantitative assessment of nerve tissue using OCT requires a thorough understanding of how light interacts with biological tissue and how we can measure those interactions.

We've demonstrated that significant information about nerve microstructure can be extracted from OCT and PS-OCT images. Given the micrometer-level spatial resolution and millimeter-level penetration depth and the methods described above, we can precisely define the epineurial boundaries and measure the epineurial thickness of

peripheral nerves. This serves as a means of defining specific regions within our OCT and PS-OCT images from which to extract additional information of. This is especially important in assessment of the internal axonal microstructure of a nerve from the outer surface. Information about the interior axonal microstructure and the surrounding muscle tissue was obtained through measurements of light attenuation and birefringence. We've shown that these two tissue types have significantly different light attenuation properties but exhibit similar amounts of birefringence. These tissues can be distinguished from one another on the basis of their measured attenuation coefficients. Additional information related to the axonal microstructure can be obtained by examining the presences of the Bands of Fontana. The visibility of these bands depends on the orientation and alignment of the axonal fibers. A slight undulation in the nerve orientation allows for differences in light scattering that manifest and dark and light bands on the nerve surface. The frequency of the appearance of these bands is a direct indication of the amount of longitudinal stress the nerve is under. We've shown that a decrease in the frequency of the bands is associated with an increase in applied longitudinal stress.

We were particularly interested in determining if a change in birefringence accompanies applied tensile stress. It's been previously demonstrated that a loss in birefringence accompanies nerve injury due to the degeneration of the myelin sheaths of the axons [59]. For nerve injury assessment, it needs to be clear that the change in birefringence is solely due to injury and not the structural state of the nerve. We demonstrated that increased application of longitudinal stress on a nerve does not change the amount of measured birefringence, indicating that the amount and organization of the

myelin remains unchanged. Longitudinal stress reduces the undulation of the axons running in parallel but doesn't change the axonal organization or density required to manifest as a change in birefringence. In the context of nerve injury assessment, this allows us to more confidently attribute changes in birefringence to the underlying injury.

Section 3.4: Conclusions

In summary, this chapter described the development of methods for making structural and functional measurements from OCT and PS-OCT image data that can be used to classify and characterize biological tissue as well as study nerve injury at a level inaccessible to any currently existing technology. Our developed methods are rooted in basic biophotonics and light-tissue interactions concepts and have enabled the boundary definition and thickness measurement of peripheral nerve epineurium, the measurement of the frequency of Bands of Fontana to inform us of the amount of longitudinal stress a peripheral nerve is experiencing and the classification and characterization of nerve and muscle tissue. Additionally, we demonstrated a constant birefringence measurement as a function of increasing applied longitudinal stress on a peripheral nerve. The combination of the developed methods and results build a framework for optically-based, minimally-invasive, high-resolution structural and functional assessment of peripheral nerve injury.

Chapter 4: Phase microscopy extensions of spectral-domain optical coherence tomography

This chapter describes the development and implementation of a phase sensitive extension of SD-OCT called spectral-domain optical coherence phase microscopy (SD-OCPM). The chapter is organized into three sections: an introduction to the theoretical bases for SD-OCPM (Section 4.1), a description of the characterization and calibration procedures for SD-OCPM systems (Section 4.2) and a demonstration of the use of SD-OCPM imaging for characterizing transient structural changes that accompany functional stimulation in neurons (Section 4.3).

Spatial resolutions of conventional OCT imaging are in the range of 1-15 μm based on the specifications of the source and sampling arm optics. This is insufficient for visualizing sub-cellular features within cellular samples. Phase extensions of OCT have been shown to provide nanometer-level resolution of the optical path length mismatch between the reference and sample arms of the interferometer. This provides us with sufficient depth resolution to resolve small phase shifts in the optical path length mismatches induced by subcellular features of cellular samples. These phase shifts are the basis for quantitative phase image reconstruction in SD-OCPM.

In traditional SD-OCT imaging, the intensity of backscattered light is used to generate microstructural images of biological tissue. Functional extensions of SD-OCT (PS-OCT and D-OCT) exploit the phase of backscattered light to generate images of tissue physiology and fluid flow respectively. However, these aren't the only uses for phase in SD-OCT-based imaging. It can be used to explore an entirely different spatial

scale of biology. In a technique called SD-OCPM, the phase is used to reconstruct quantitative, label-free images of entire cells and sub-cellular features [60,61,62,63]. Cells are placed on highly reflective glass coverslips and imaged with an SD-OCT system. The coverslip works as the interferometer where the sample surface is the coverslip surface with the cell on it and the reference surface is the other surface of the coverslip (often referred to as a common path geometry) [62,64,65,66,67,68,69,70]. The phase of each of these surfaces is extracted and subtracted from each other to determine the additional optical path length experienced by the photons due to interaction with the cell. The common path geometry found in traditional SD-OCPM results in excellent phase stability and allows for resolving optical path length mismatches down to the picometer level. However, this restricts the types of samples and experiments that can be run. Samples are typically fixed static cells mounted on coverslips for cellular and subcellular structural analysis only.

Our solution to overcoming the restrictions offered by traditional SD-OCPM imaging is to redesign the interferometer of the SD-OCT system to allow us to perform live cell imaging. Traditional SD-OCPM requires the reference surface to be very near the sample surface within the same arm of the interferometer. We propose to remove this requirement by moving the interferometer just before the final lens in the sample arm to maintain as common a path as possible for the light through the system (Figure 4.1).

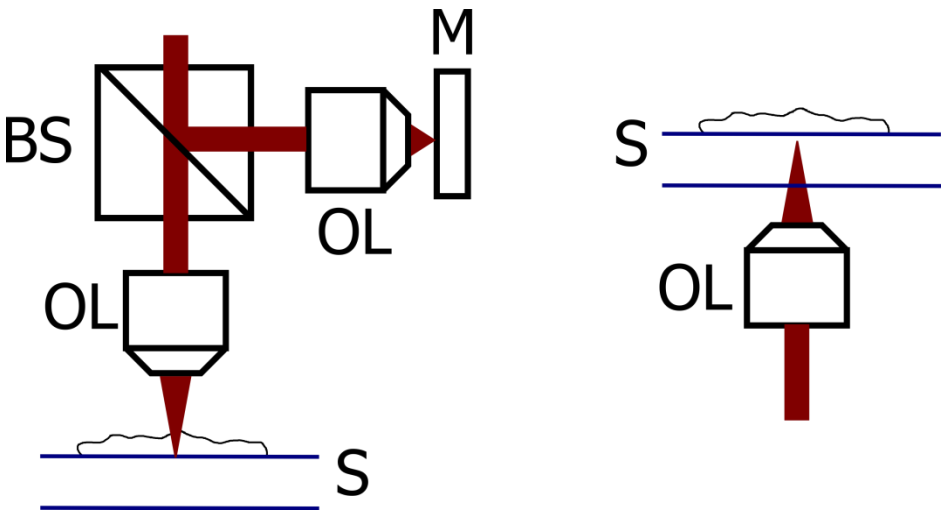

Figure 4.1: Schematics of our SD-OCPM setup (left) and the conventional SD-OCPM setup (right). BS: beam splitter, M: mirror, OL: objective lens, S: sample

Additionally, we use a water immersion objective as our final lens for light delivery and collection and to facilitate live cell imaging. These modifications maintain a relatively low phase noise floor while offering the ability to perform live cell imaging and analyze dynamic cellular physiology. The movement of the interferometer results in an increase phase noise floor that necessitates the development of alternative phase stabilization techniques to accurately reconstruct quantitative phase images of live cellular samples.

Section 4.1: Theory

SD-OCPM is based on SD-OCT and includes additional processing steps for phase image reconstruction. Following the convention of Joo et al. [62], the spectral interference detected at the spectrometer for an incident beam at a position (x,y) on the surface of a sample is given by:

$$I(k)\big|_{(x,y)} = 2\sqrt{R_r R_s(z)}S(k)\cos\left(2k\Delta p(z)\right)\big|_{(x,y)} \tag{4.1}$$

where k is the wavenumber, R_r is the reference reflectivity, $R_s(z)$ is the sample reflectivity at depth z, $S(k)$ is the source power spectral density and $\Delta p(z)$ is the optical path length difference between the reference and sample arms at depth z. A Fourier transform of this spectral interferogram results in a complex value depth profile from which the phase (in units of radians) can be extracted from:

$$\phi(z)\big|_{(x,y)} = \tan^{-1}\left(\frac{Im\left[\mathcal{F}(z)\right]}{Re\left[\mathcal{F}(z)\right]}\right) = 2\left(\frac{2\pi}{\lambda_o}\right)\Delta p(z) \tag{4.2}$$

$\mathcal{F}(z)$ is the Fourier transform of the spectral interferogram and λ_o is the center wavelength of the source. The phase of the depths that correspond to the two surfaces of the coverslip are extracted and subtracted from one another. The extracted phase difference is wrapped between $\pm\pi$ and requires phase unwrapping routines to extract the true optical path length mismatch used to reconstruct quantitative phase images of a cell. As mentioned earlier, using the coverslip as the interferometer of the SD-OCPM system results in a system with excellent phase stability and allows for resolving optical path length mismatches at the picometer level but is restrictive in terms of the types of samples and experiments that can be run. An SD-OCPM system capable of imaging live cell samples would allow for the quantitative examination of cellular physiology in response to various stimuli and be of significant utility to the medical and life sciences research community.

Section 4.2: System calibration and characterization

Our SD-OCPM setup consists of a fiber-based spectral-domain optical coherence tomography imaging system built into an upright microscope equipped for bright field and fluorescence microscopy (Figure 4.2). Light from a Ti-Saph laser (λ_o = 800 nm, $\Delta\lambda$ = 170 nm, FemtoLasers, Inc.) is delivered to the sample by an upright microscope (Olympus BX61WI). Raster scanning of the beam is done via a pair of galvanometer scanning mirrors (Cambridge 6210H). The interferometer of the system is installed into the microscope to maintain as common a path for light propagation as possible. A 70:30 unpolarized beam splitter splits the light between reference and sample arms. The reference arm consists of an objective (Olympus PLN 20X, 0.4 NA) and a mirror. The sample arm consists of a water immersion objective (Olympus UMPlanFLN 20X, 0.5 NA) for light delivery and collection and allows for live cell imaging. The recombined beams are sent to a custom built spectrometer for detection. The spectrometer consists of a transmission diffraction grating (600 lines/mm), a focusing lens (f = 151.4 mm) and a 4096 element line scan camera (Basler Sprint spL4096-70k, 8-bit resolution). The axial and lateral resolutions of the system were measured to be 1.85 μm and 4.34 μm respectively.

The bright-field microscopy (BM) system used for verification is built into the same upright microscope. The lamp installed into the upright microscopes serves as the illumination source and is collected by the same objective as the SD-OCPM system. The transmitted light is incident on a dichroic mirror emission filter (535/50, Chroma) and

sent to an EM-CCD for detection (Hamamatsu EM-CCD C9100-02, 14-bit resolution). The lateral resolution of the BM system was measured to be 1.86 μm.

The SD-OCPM and BM imaging systems are controlled by a single workstation running Windows 7 64-bit and equipped with a multi-core processor (2.5 GHz Intel Xeon E5-2640), 32 GB RAM, three high-performance frame grabbers (two NI PCIe-1429 and one Active Silicon Phoenix D24CL PE1) controlling the two line scan cameras and the EM-CCD respectively and a high speed multifunction data acquisition card (NI PCIe-6259, 16-bit resolution. 1.25 MS/s) for sending out the driving waveforms for the galvanometer scanning mirrors, line scan cameras and EM-CCD. The software application managing both systems is a multi-threaded application developed in Visual C++ using Microsoft Visual Studio 2008. Separate threads control the computation of the driving waveforms and the acquisition, processing and saving of data from the line scan cameras and EM-CCD.

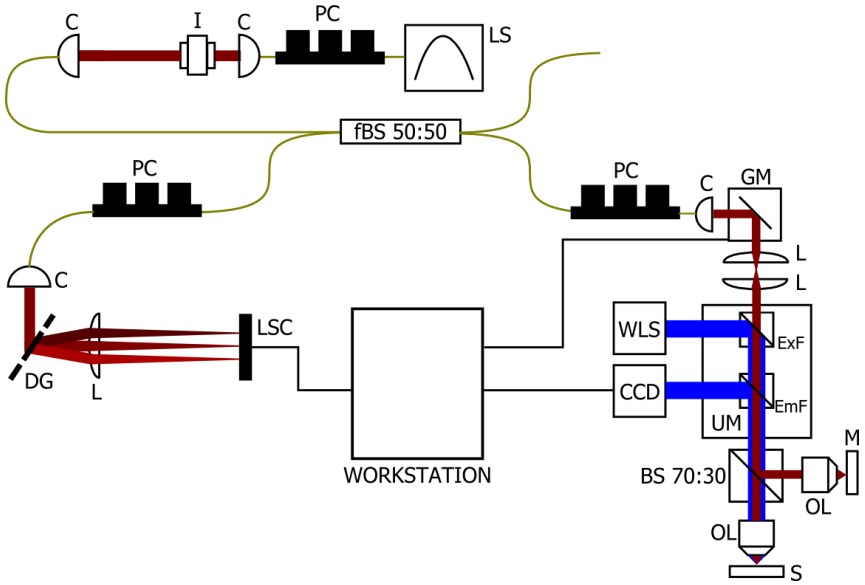

Figure 4.2: System diagram of the combined SD-OCPM-BF imaging system centered at 800 nm. LS: laser source, PC: polarization controller, C: collimator, I: isolator, fBS: 50/50 beam splitter, GM: galvo mirrors, L: lens, BS: beam splitter, M: mirror, OL: objective lens, S: sample, DG: diffraction grating, LSC: line scan camera, WLS: white light source. ExF: excitation filter, EmF: emission filter.

Section 4.2.1: Calibration

Proper calibration of the spectrometer in the SD-OCPM system is crucial to obtaining excellent SD-OCPM data. As mentioned previously, spectral interferograms are typically unevenly spaced in wavenumber and require remapping to evenly spaced wavenumbers to avoid the broadening of the axial point spread function (aPSF) that reduces the axial resolution of SD-OCT systems [13]. Proper calibration involves accurate assessment of the wavelengths that correspond to each element on the line scan camera in the spectrometer and pre-processing of the associated wavenumbers such that they are evenly spaced in *k*-space. We followed the auto-calibration technique of Mujat et al. [71] to perform accurate wavelength mapping for calibration of the spectrometer in

our SD-OCPM system. Briefly, proper wavelength assignment of the pixels on the line scan camera of the spectrometer can be obtained by imposing a known *k*-dependent modulation onto the detected spectrum. A microscope coverslip placed into the source arm of the system imposes a perfect sinusoidal modulation with a frequency related to the optical path length mismatch between light internally reflected twice between its surfaces. For a perfect sinusoidal function, the phase of the oscillation should be linearly related to *k*. Incorrect wavelength mapping will result in a non-linear relationship between the phase and *k*. An initial estimate of the wavelength assignment on the spectrometer is determined using the grating equation based on the design of our spectrometer. Next, these wavelengths are converted to *k*-space and interpolated to obtain an evenly-spaced *k*. Using the criteria that a perfectly sinusoidal modulation should exhibit a linear relationship between the phase and *k*, these wavenumbers are iteratively corrected by minimizing the nonlinearity in the phase under the assumption that this is entirely due to an incorrect wavelength assignment.

The design of our SD-OCPM system required an additional calibration step to correct for the dispersion mismatch between the reference and sample arms of the interferometer. A dispersion mismatch results in broadening of the aPSF similar to incorrect wavelength assignment of the spectrometer. We followed the numerical dispersion compensation technique of Wojtkowski et al. [72] to correct out the dispersion mismatch between the reference and sample arms and sharpen our aPSF. Briefly, a correct wavelength assignment for the spectrometer results in a linear relationship between the phases of the modulation imposed on the spectrum and wavenumber. A

dispersion mismatch introduces an additional non-linearity in the phase vs. wavenumber relationship. By placing a perfect reflector in the sample arm and examining the phase of the imposed modulation on the spectrum, we can determine the non-linearity introduced by the dispersion mismatch and compute correction factors to recover the linear relationship between the phase of the modulation imposed on the spectrum and wavenumber. By performing proper wavelength assignment and correcting for the dispersion mismatch in our interferometer, we obtain an axial resolution of 1.85 μm that matches well with the theoretical axial resolution provided by the specifications of our light source (1.66 μm).

Section 4.2.2: Characterization

SD-OCPM systems can be limited by three main types of noise: readout and dark noise, shot noise and relative-intensity (RIN) noise. A shot noise-limited system provides the best performance because it is a fundamental noise source related to the statistical fluctuation of photon counts by the detector. To determine the noise limit of our system, we stepped the intensity level on our spectrometer with a neutral-density filter and examined the relationship between the standard deviation of the intensity and average intensity (Figure 4.3).

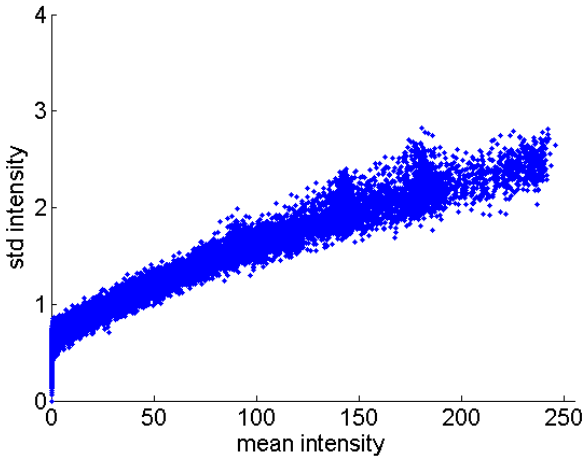

Figure 4.3: Standard deviation intensity vs. average intensity plot to determine noise limit of the SD-OCPM system. A linear relationship indicates a shot-noise limited system.

Readout and dark noise-limited systems exhibit a constant relationship, shot noise-limited systems exhibit a linear relationship and RIN noise-limited systems exhibit a non-linear relationship between the standard deviation and average intensity respectively. Our SD-OCPM is shot noise-limited due to the linear relationship between the standard deviation and average intensity (Figure 4.3).

One issue inherent to SD-OCT-based imaging is the non-uniform SNR over the entire depth scan range. As the path length mismatch between the reference and sample arms increases, the SNR decreases due to the finite spectral resolution of the spectrometer. We followed the technique of Yun et al. [73] to characterize the SNR drop-off and measure the spectral resolution of our system. A mirror was placed in the sample arm and the SNR of the peak corresponding to the mirror was measured as a function of the optical path length mismatch between the reference and sample arms (Figure 4.4).

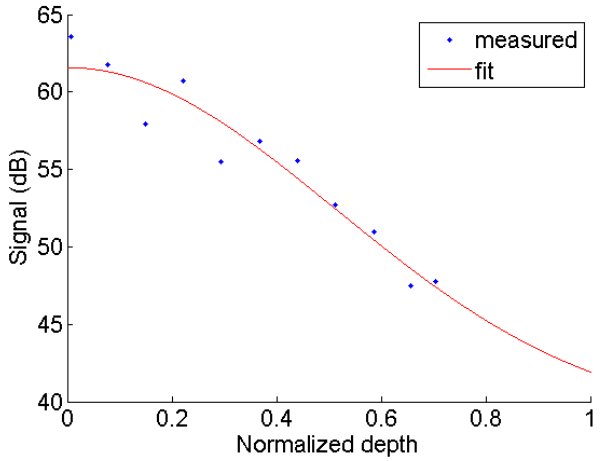

Figure 4.4: Measured sensitivity drop-off of the SD-OCPM system. Blue data points represent experimental measurements and the red line represents the fit using (4.3).

The magnitude of the sensitivity drop-off can be described by the following equation:

$$R(z) = A + B\left(\frac{\sin\zeta}{\zeta}\right)^2 \exp\left(-\frac{w^2}{2ln2}\zeta^2\right) \tag{4.3}$$

where A and B are fitting parameters, $\zeta = (\pi/2)\cdot(z/z_{RD})$ and describes the depth normalized to the maximum imaging depth, $z_{RD} = \lambda^2/4\Delta\lambda$, $w = \delta\lambda/\Delta\lambda$, $\Delta\lambda$ is the wavelength spacing between pixels on the line scan camera and $\delta\lambda$ is the spectral resolution of the spectrometer. Using 4.3 to fit the sensitivity drop-off data yield a spectral resolution of 0.061 nm.

The phase noise of our system directly affects our ability to measure the nanometer-level optical path length mismatches of the interferometer necessary to reconstruct quantitative phase images. The optimal phase noise floor of an SD-OCPM system is achieved at maximal SNR and no mechanical beam steering by the galvo mirrors in the sample arm. We followed the techniques of Park et al. [35] to characterize the phase noise floor as a function of SNR of our SD-OCPM system. To quantify this

relationship, 1024 interference spectra of a single point on a microscope cover slip were acquired at different SNRs achieved using a neutral density filter in the sample arm. The standard deviation of the phase difference (the minimum detectable phase difference) between the two surfaces of the coverslip was computed as a measure of the phase noise floor at different SNRs (Figure 4.5).

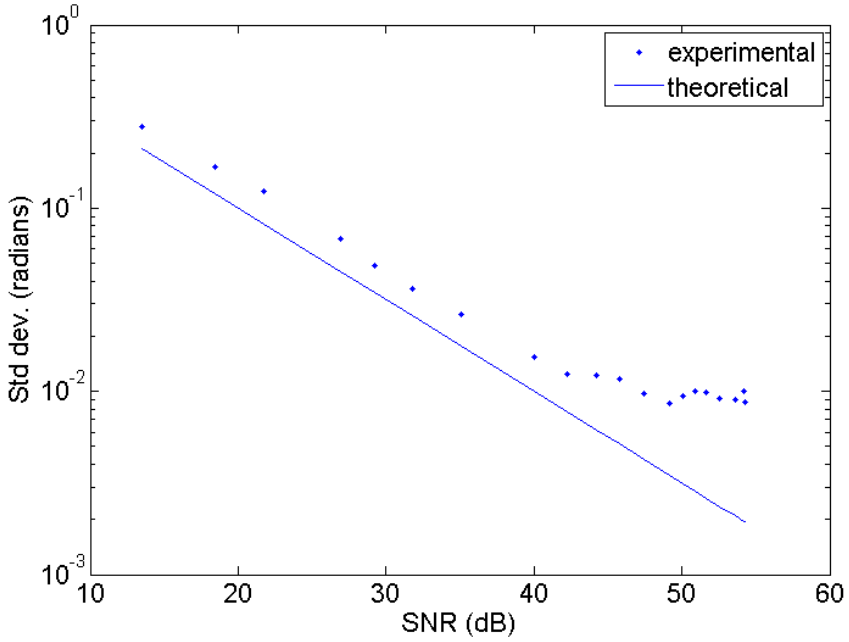

Figure 4.5: Phase noise vs. SNR plot for the SD-OCPM system. Dots represent measured phase noise at the given SNR and the solid blue line represents the theoretical phase noise at the given SNR.

Two conclusions can be drawn from the relationship between the minimum detectable phase difference and SNR: (1) after an SNR of ~40 dB, the phase noise floor reaches a plateau and no additional advantage is offered at higher SNRs and (2) a constant offset between the theoretical and experimental phase noise measurements exists. One can infer that an SNR-independent source of noise exists that explains the constant noise offset from theoretical as well as the SNR at which the phase noise floor plateaus. A thorough

analysis of possible noise sources led us to determine that vibrations in the optical table are the source of the offset and beginning of the phase noise floor plateau.

Section 4.3: Single cell imaging using SD-OCPM

Quantitative phase microscopy using the SD-OCPM system described above was demonstrated by structural imaging of cheek epithelial cells and imaging and quantitative analysis of morphological changes in neurons after functional stimulation via glutamate. The modifications proposed above to gain the ability to perform dynamic live cell quantitative phase microscopy require a specialized phase image reconstruction work flow to obtain quantitative phase images. As mentioned earlier, the phases of the depths that correspond to the cover slip surfaces are extracted for analysis. Instead of subtracting the phases of the two coverslip surfaces, only the phase from the surface containing the cell is used for reconstruction. The phase from this surface is wrapped between $\pm \pi$ and requires phase unwrapping to yield the true optical path length mismatch. Given that all the A-lines in a given B-line are acquired on a continuous clock and that B-line acquisitions are independent from each other, we performed one-dimensional phase unwrapping of the phases extracted from the top surface of the coverslip within each B-line for all B-lines that comprise the imaging volume. The result is a series of one-dimensionally unwrapped phases that represent the optical path length mismatches between the top surface of the coverslip and the reference arm of the interferometer and the additional optical path length due to the presence of the cell. These one-dimensionally unwrapped phases are slightly offset with respect to each other and show

that the imaged glass surface is slightly tilted. A weighted polynomial fit of the unwrapped phases in each B-line is computed and subtracted away to correct for the offset between B-lines and overall tilt of the glass surface. The glass and cell regions of the image were determined by masking the *en face* intensity image of the cell. The order of the polynomial fit as well as the weights for the glass and cell regions were determined via an optimization routine that sought to minimize the root-mean-square deviation (RMSD) of the difference between the unwrapped phase image from the top coverslip surface to the unwrapped phase image from traditional SD-OCPM. This allows us to correct out the artifacts due to the relative B-line phase offsets and overall tilt of the glass surface while preserving the phase information of the cell itself.

As a first demonstration of the capabilities of the system and phase image reconstruction workflow, cheek epithelial cells on a microscope cover slip were simultaneously imaged with SD-OCPM and BM. A cheek swab from a healthy volunteer was performed and epithelial cells transferred to a coverslip for imaging. A small amount of water was added to the top of the coverslip for contact with the water immersion objective in the sample arm of the SD-OCPM system. 512 x 512 spectra were acquired over an area covering 50 x 50 μm of physical space at a line rate of 10 kHz. A BM image was taken to verify the accuracy of the image obtained from the SD-OCPM system.

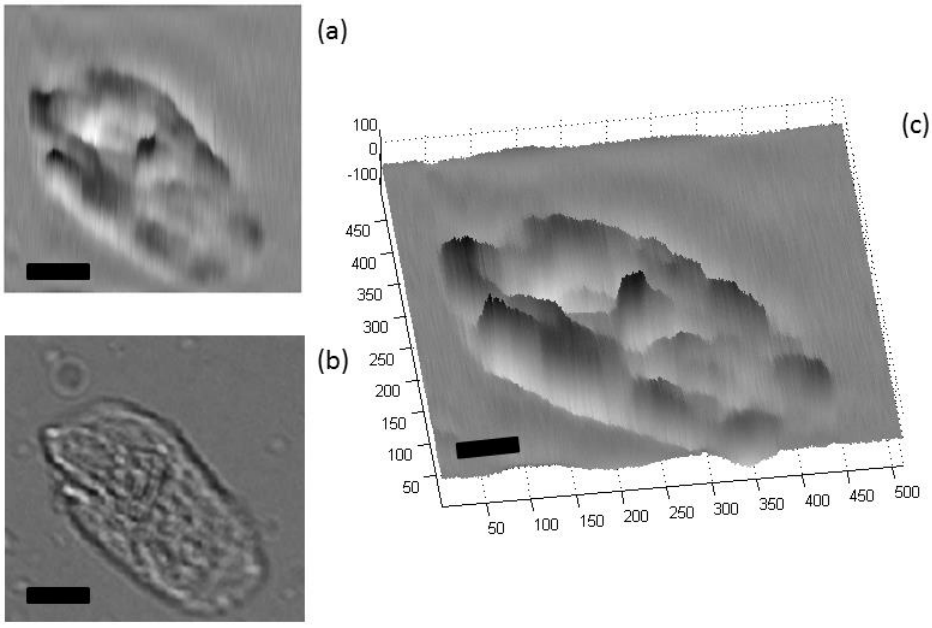

Figure 4.6: SD-OCPM and BM images of a cheek epithelial cell. (a) SD-OCPM image, (b) BM image, (c) topological SD-OCPM image demonstrating how optical path length mismatches can be used to profile the surface of the cell. X and Y axes are in units of pixels. Z axis is in units of nanometers. Scale bar: 10 μm.

Our data shows that our system and phase image reconstruction work flow can successfully and accurately reconstruct quantitative phase images (Figure 4.6). The cheek epithelial cell morphology seen in the SD-OCPM image (Figure 4.6a) matches well with the morphology seen in the BM image (Figure 4.6b). In addition to accurate morphology, SD-OCPM images are inherently quantitative with each pixel value representing the optical path length mismatch at that spatial location. This allows for topological reconstruction of the data to look at the surface profile of the cell and access to a spatial dimension that is inaccessible with BM (Figure 4.6c). It also enables us to assess morphological changes in single cells across all three spatial dimensions.

Demonstration of the capabilities of the system to reconstruct quantitative phase images and measure morphological changes in a cell was done by imaging single neurons on a microscope cover slip before and after the application of the neurotransmitter glutamate to the culture media. 512 x 512 spectra were acquired over 50 x 50 µm area at a line rate of 10 kHz (~1 frame/min). Simultaneous BM images were taken at a frame rate of 1 Hz to verify the morphological changes induced by the addition of 100 µL of 1 M glutamate to the 2 mL of culture media. SD-OCPM and BM images were acquired over a period of five minutes to establish baseline neuron morphology followed by one hour of post-glutamate SD-OCPM and BM imaging to assess glutamate-induced morphological changes in the neuron.

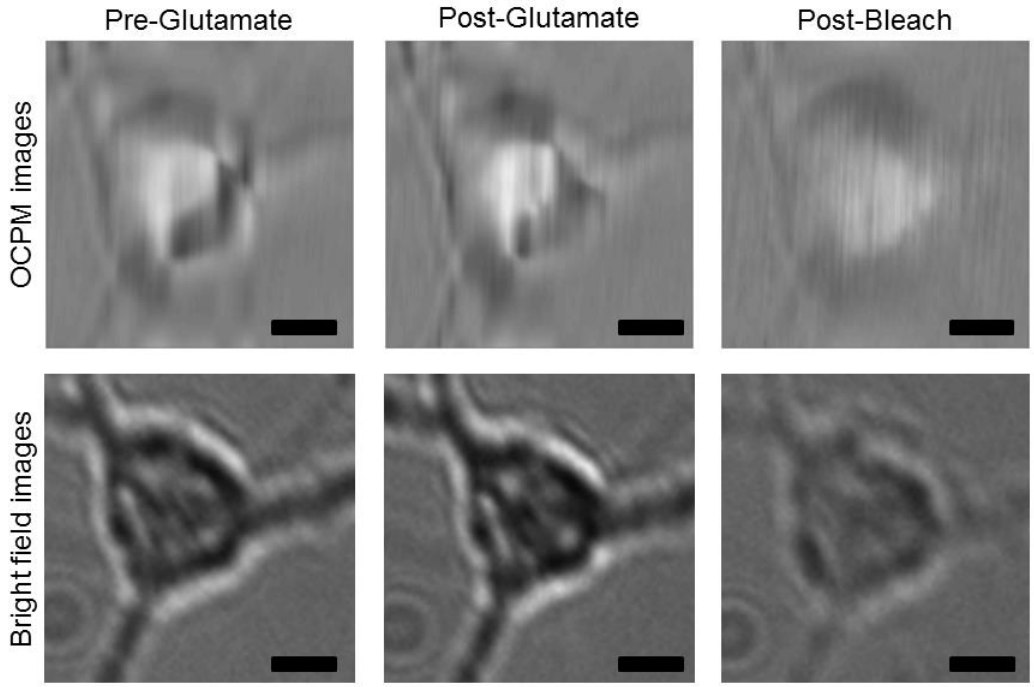

Figure 4.7: SD-OCPM and BM images of a single neuron. The top row consists of SD-OCPM images of a single neuron before Glutamate, after Glutamate and after bleach addition. The bottom row consists of the BM images for the same conditions. Bar: 10 µm

Single SD-OCPM and BM images before and after the addition of glutamate are shown in Figure 4.7. The morphology of the neurons seen in the SD-OCPM images (Figure 4.7) matches well with the morphology of the neurons seen in the BM images (Figure 4.7).

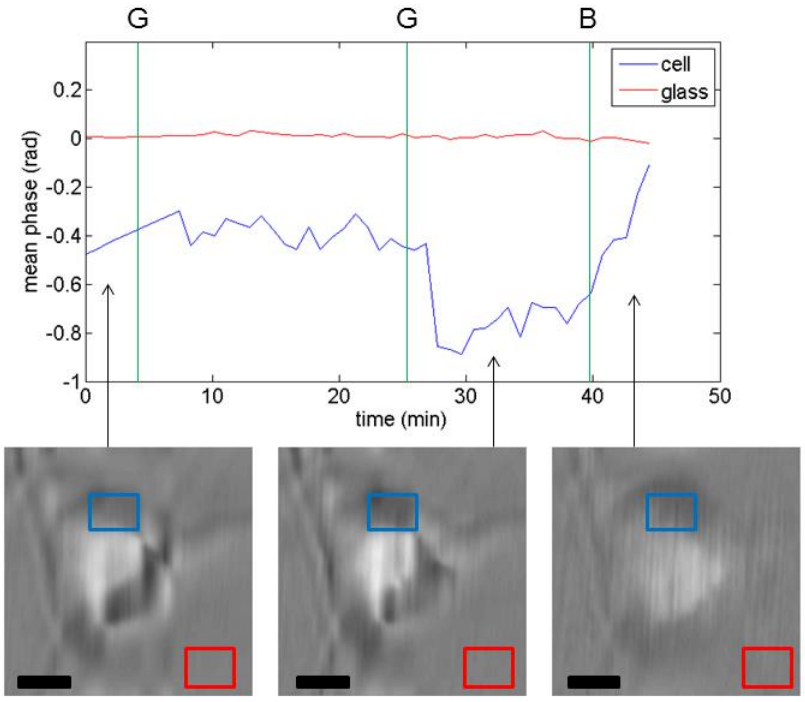

Figure 4.8: Quantitative analysis of phase shifts induced via the addition of Glutamate. Blue squares identify the regions of the images used to monitor the phase behavior within the neuron. Red squares identify the regions of the images used to monitor the phase behavior of the glass. Green lines indicate the times at which Glutamate or bleach was added to the culture media. G: Glutamate addition, B: bleach addition. Bar: 10 µm

The quantitative aspects of SD-OCPM imaging allow us to assess morphological changes across all three spatial dimensions. We analyzed phase changes in small regions of interest (ROIs) corresponding to the microscope cover slip and neuron. The phase trends in the cover slip ROI acts as control phase data to ensure that the addition of glutamate doesn't induce optical path length changes. The phase trends in the neuron ROI

allow us to quantitatively assess morphological changes in the axial direction in response to the addition of glutamate. The phase trends in both ROIs remains constant before the addition of glutamate. After glutamate is added to the culture media, the phase trend in the cover slip ROI remains constant while the phase trend in the neuron ROI changes over the duration of the experiment (Figure 4.8).

Section 4.4: Discussion

The most well-known optical contrast is fluorescence. Getting fluorescence contrast of a biological sample typically requires the application of an exogenous dye targeted to a specific biological moiety or genetically encoding a fluorescent protein to the gene/protein of interest. This has been an invaluable tool in the study of a plethora of fields across the medical and life sciences. Another advantage to using fluorescence as a contrast is it offers some degree of quantitative analysis because the strength of the fluorescence can be traced to the concentration of the underlying fluorophore. Another popular method of achieving contrast is to exploit the phase of light waves. The basis for phase contrast is in the differing refractive indices of biological materials. Phase contrast is attractive because it requires no exogenous application or genetic encoding of contrast agents like fluorescence but typically lacks quantitative information without additional system complexity. The combination of the quantitative measurements possible with fluorescence microscopy with the label-free contrast of phase microscopy into a single imaging modality would be a powerful tool for quantitative, label-free and dynamic analysis of cellular physiology across cell types.

SD-OCPM combines the advantages of label-free imaging inherent to refractive index-based contrast with quantifiable optical path length mismatches measurable by SD-OCT. A requirement for SD-OCPM imaging of single cells is the ability to resolve optical path length mismatches on the order of a few hundred nanometers (the approximate height of a cell). This requires an SD-OCPM system with high spatial resolutions and a low phase noise floor as well as an image reconstruction work flow that can process a series of interference spectra into quantitative phase images. The phase measured by an SD-OCPM system is an ensemble average of the phases of the photons reflected back from a small sample volume defined by the spatial resolutions of the system. Measuring reliable phase information is based on two main factors that affect the phase noise floor of an SD-OCPM system: SNR and lateral beam scanning [35]. Higher SNR and increased beam overlap during lateral scanning result in lower phase noise. A careful balance of imaging speed, physical scan range and spatial sampling (number of A-lines per image and number of images per volume) must be considered to ensure the optimal phase noise for SD-OCPM imaging of cellular samples.

Here we've summarized our work on the improvement of SD-OCPM for dynamic live cell imaging and application of SD-OCPM for morphological visualization of cheek epithelial cells and examination of functionally stimulated morphological changes in neurons. In all cases, the cell morphology seen in the SD-OCPM images match well with the cell morphology seen in the BM images. Results show that addition of high concentrations of glutamate induces morphological changes in neurons that can be visualized and quantified simultaneously in SD-OCPM and bright field images. SD-

OCPM image analysis demonstrates that these changes occur in three dimensions and that changes in the height of the cell can be directly measured and quantified by examining changes in the optical path length mismatch.

Section 4.5: Conclusions

In summary, this chapter described the improvements on SD-OCPM for performing dynamic quantitative live cell phase microscopy and the application of SD-OCPM for quantitatively assessing morphological changes in single neurons in response to the application of glutamate. SD-OCPM combines the advantages of label-free imaging inherent to refractive index-based contrast with quantifiable optical path length mismatches measurable by SD-OCT allowing us to quantitatively examine cellular morphology across all three spatial dimensions without exogenous contrast agents. We described and characterized our SD-OCPM imaging system and demonstrated its utility in the visualization and analysis of morphological changes in single neurons in response to the addition of glutamate. This type of imaging system is well-suited to study dynamic cellular physiology in a variety of cell types and further demonstrates the versatility of the SD-OCT technology for imaging both tissue samples and cellular samples.

Conclusion

In summary, this dissertation has described the development of a GPU-accelerated MF-SD-OCT imaging system capable of high-speed imaging of biological tissue, the application of MF-SD-OCT for imaging, visualization and analysis of peripheral nerve and muscle tissue and the improvement of SD-OCPM for imaging, visualization and analysis of single cheek epithelial cells and single neurons. This demonstrates the versatility of the OCT technology for imaging biological samples across spatial scales with intrinsic contrast and quantitatively analyzing image data for making a variety of important biological measurements.

A GPU-accelerated MF-SD-OCT system enables rapid structural and functional assessment of biological samples and monitoring of fast dynamic biological phenomena across all spatiotemporal dimensions. The CUDA programming platform used to develop the GPU-accelerated MF-SD-OCT data processing algorithms allows for transparent scalability of kernel execution across generations of GPU devices, enabling easy hardware upgrades to obtain additional performance enhancements. This would allow additional SD-OCT-based processing to be incorporated into the software and extend the on-line processing capabilities of the MF-SD-OCT system and software.

The development of a technologically-advanced MF-SD-OCT imaging system enables the application of the technology for exploring meaningful applications in the life sciences. Quantitative biophotonics-based structural and functional measurements from OCT and PS-OCT image data can be used to classify and characterize biological tissue as well as study nerve injury at a level inaccessible to any currently existing technology.

These classification and characterization methods are applicable to a wide range of biological tissue samples and describe the interactions of light and biological matter at the tissue level. Understanding the micro-scale interactions between light and biological matter that contribute to the macro-scale optical properties at the tissue level requires a resolution beyond that of conventional MF-SD-OCT.

The SD-OCPM extension of SD-OCT is capable of resolving nanometer-level optical path length mismatches that can be used to achieved the cellular-level resolution necessary to explore micro-scale contributions to macro-scale optical properties at the tissue level. An improvement on traditional SD-OCPM for performing dynamic, quantitative, label-free, live cell phase microscopy enables the quantitative assessment of morphological changes in a variety of cell types across all spatiotemporal dimensions and is a crucial step towards examining light-matter interactions at the cellular level.

The development of an advanced versatile SD-OCT-based imaging system and sophisticated MF-SD-OCT processing work flows and measurement methods make OCT an extremely powerful tool for applications across the life sciences. As demonstrated in the text of this dissertation, OCT is capable of performing quantitative, label-free, high-speed high-resolution imaging across spatial scales, enabling the examination of unaltered dynamic tissue and cellular physiology. Just as magnetic resonance imaging revolutionized the study of the human body beginning in the 1970s, OCT has the potential to produce the next generation of breakthroughs in the medical and life sciences fields.

References

[1] Huang, D., Swason, E. A., Lin, C. P., Schuman, J. S., Stinson, W. G., Chang, W., Hee, M. R., Flotte, T., Gregory, K., Puliafito, C. A., and Fujimoto, J. G. (1991). Optical coherence tomography. *Science,* 254(5035):1178–81.

[2] Izatt, J. A., and Choma, M. A. *Theory of Optical Coherence Tomography* in *Optical Coherence Tomography – Technology and Applications*. Drexler, W., and Fujimoto, J. G. Editors (Springer-Verlag Berlin Heidelberg, 2008).

[3] Swanson, E. A., Izatt, J. A., Hee, M. R., Huang, D., Lin, C. P., Schuman, J. S., Puliafito, C. A., and Fujimoto, J. G. (1993). In-vivo retinal imaging by optical coherence tomography. *Optics Letters,* 18(21):1864-66.

[4] Hee, M. R., Puliafito, C. A., Wong, C., Duker, J. S., Reichel, E., Rutledge, B., Schuman, J. S., Swanson, E. A., and Fujimoto, J. G. (1995). Quantitative assessment of macular edema with optical coherence tomography. *Archives of Ophthalmology,* 113(8):1019-29.

[5] Drexler, W., Morgner, U., Ghanta, R. K. , Kartner, F. X., Schuman, J. S., and Fujimoto, J. G. (2001). Ultrahigh-resolution ophthalmic optical coherence tomography. *Nature Medicine,* 7(4):502-07.

[6] Pierce, M. C., Park, B. H., Cense, B., and de Boer, J. F. (2002). Simultaneous intensity, birefringence, and flow measurements with high-speed fiber-based optical coherence tomography. *Optics Letters,* 27(17):1534-36.

[7] Fercher, A. F., Hitzenberger, C. K., Kamp, G., and El-Zaiat, S. Y. (1995). Measurement of intraocular distances by backscattering spectral interferometry. *Optics Communications,* 117(1-2):43-48

[8] Mitsui, T. (1999). Dynamic range of optical reflectometry with spectral interferometry. *Japanese Journal of Applied Physics,* 38:6133-37

[9] Yun, S., Tearney, G. J., de Boer, J. F., Iftimia, N., and Bouma, B. E. (2003). High-speed optical frequency-domain imaging. *Optics Express,* 11(22):2953-63.

[10] Leitgeb, R., Hitzenberger, C. K., Fercher, A. F. (2003). Performance of Fourier domain vs. time domain optical coherence tomography. *Optics Express,* 11(8):889–94.

[11] de Boer, J. F., Cense, B., Park, B. H., Pierce, M. C., Tearney, G. J. and Bouma, B. E. (2003). Improved signal-to-noise ratio in spectral-domain compared with time-domain optical coherence tomography. *Optics Letters,* 28(21):2067–69.

[12] Choma, M. A., Sarunic, M. V., Yang, C. H. and Izatt, J. A. (2003). Sensitivity advantage of swept source and Fourier domain optical coherence tomography. *Optics Express,* 11(18):2183–89.

[13] Wojtkowski, M., Leitgeb, R., Kowalczyk, A., Bajraszewski, T., and Fercher, A. F. (2002). *In vivo* human retinal imaging by Fourier domain optical coherence tomography. *Journal of Biomedical Optics,* 7(3):457-63.

[14] Hee, M. R., Huang, D., Swanson, E. A., and Fujimoto, J. G. (1992). Polarization-sensitive low-coherence reflectometer for birefringence characterization and ranging. *Journal of the Optical Society of America B,* 9(6):903–9.

[15] de Boer, J. F., Milner, T. E., van Gemert, M. J. C., and Nelson, J. S. (1997). Two-dimensional birefringence imaging in biological tissue by polarization-sensitive optical coherence tomography. *Optics Letters,* 22(12):934–6.

[16] de Boer, J. F., Milner, T. E., and Nelson, J. S. (1999). Determination of the depth-resolved Stokes parameters of light backscattered from turbid media by use of polarization-sensitive optical coherence tomography. *Optics Letters,* 24(5):300–2.

[17] Cense, B., Chen, T. C., Park, B. H., Pierce, M. C., and de Boer, J. F. (2004). Thickness and birefringence of healthy retinal nerve fiber layer tissue measured with polarization-sensitive optical coherence tomography. *Investigative Ophthalmology and Visual Science,* 45(8):2606-12.

[18] de Boer, J. F., Milner, T. E. (2002). Review of polarization sensitive optical coherence tomography and Stokes vector determination. *Journal of Biomedical Optics,* 7(3):359–71.

[19] Park, B. H., Pierce, M. C., Cense, B., and de Boer, J. F. (2004). Jones matrix analysis for a polarization-sensitive optical coherence tomography system using fiber-optic components. *Optics Letters,* 29(21):2512–4.

[20] Park, B. H., Pierce, M. C., Cense, B., and de Boer, J. F. (2005). Optic axis determination accuracy for fiber-based polarization-sensitive optical coherence tomography. *Optics Letters,* 30(19):2587–9.

[21] Saxer, C. E., de Boer, J. F., Park, B. H., Zhao, Y., Chen, Z., and Nelson, J. S. (2000). High-speed fiber-based polarization-sensitive optical coherence tomography of *in vivo* human skin. *Optics Letters,* 25(18):1355-57.

[22] Yasuno, Y., Makita, S., Sutoh, Y., Itoh, M., and Yatagai, T., (2002). Birefringence imaging of human skin by polarization-sensitive optical coherence tomography. *Optics Letters,* 27(20):1803-05.

[23] de Boer, J. F., Srinivas, S. M., Malekafzali, A., Chen, Z., and Nelson, J. S. (1998). Imaging thermally damaged tissue by polarization sensitive optical coherence tomography. *Optics Express,* 3(6):212–8.

[24] Park, B. H., Saxer, C., Srinivas, S. M., Nelson, J. S., and de Boer, J. F. (2001). *In vivo* burn depth determination by high-speed fiber-based polarization sensitive optical coherence tomography. *Journal of Biomedical Optics,* 6(4):474–9.

[25] Srinivas, S. M., de Boer J. F., Park, B. H., Keikhanzadeh, K., Huang, H. E., Zhang, J., Jung, W. Q., Chen, Z., and Nelson, J. S. (2004). Determination of burn depth by polarization-sensitive optical coherence tomography. *Journal of Biomedical Optics,* 9(1):207–12.

[26] Cense, B., Chen, T. C., Park, B. H., Pierce, M. C., and de Boer, J. F. (2002). *In vivo* depth-resolved birefringence measurements of the human retinal nerve fiber layer by polarization-sensitive optical coherence tomography. *Optics Letters,* 27(18):1610–2.

[27] Park, B. H. (2005). Fiber-based polarization-sensitive optical coherence tomography. [Dissertation]. Irvine: University of California, Irvine

[28] Chen, Z., Milner, T. E., Dave, D., and Nelson, J. S. (1997). Optical Doppler tomographic imaging of fluid flow velocity in highly scattering media. *Optics Letters,* 22(1):64–66.

[29] Chen, Z., Milner, T. E., Srinivas, S., Wang, X., Malekafzali, A., van Gemert, M. J. C., and Nelson, J. S. (1997). Noninvasive imaging of in vivo blood flow velocity using optical Doppler tomography. *Optics Letters*, 22(4):1119–21.

[30] Ren, H., Brecker, K. M., Ding, Z., Zhao, Y., Nelson, J. S. and Chen, Z. P. (2002). Imaging and quantifying transverse flow velocity with the Doppler bandwidth in a phase-resolved functional optical coherence tomography. *Optics Letters*, 27(6):409–11.

[31] Izatt, J. A., Kulkarni, M. D., Yazdanfar, S., Barton, J. K., and Welch, A. J. (1997). In vivo bidirectional color Doppler flow imaging of picoliter blood volumes using optical coherence tomography. *Optics Letters*, 22(18):1439–41.

[32] van Leeuwen, T. G., Kulkarni, M. D., Yazdanfar, S., Rollins, A. M., and Izatt, J. A. (1999). High-flow-velocity and shear-rate imaging by use of color Doppler optical coherence tomography. *Optics Letters,* 24(22):1584–86.

[33] Zhao, Y. H., Chen, Z. P., Saxer, C., Xiang, S. H., de Boer, J. F., and Nelson, J. S. (2000). Phase-resolved optical coherence tomography and optical Doppler tomography for imaging blood flow in human skin with fast scanning speed and high velocity sensitivity. *Optics Letters,* 25(2):114-16.

[34] Zhao, Y. H., Chen, Z. P., Saxer, C., Shen, Q. M., Xiang, S. H., de Boer, J. F., and Nelson, J. S. (2000). Doppler standard deviation imaging for clinical monitoring of in vivo human skin blood flow. *Optics Letters,* 25(18):1358-60.

[35] Park, B. H., Pierce, M. C., Cense, B., Yun, S., Mujat, M., Tearney, G. J., Bouma, B. E., and de Boer J. F. (2005). Real-time fiber-based multi-functional spectral-domain optical coherence tomography at 1.3 μm. *Optics Express,* 13(11):3931-44.

[36] Schaefer, A. W., Reynolds, J. J., Marks, D. L., and Boppart, S. A. (2004). Real-time digital signal processing-based optical coherence tomography and Doppler optical coherence tomography. *IEEE Transactions on Biomedical Engineering,* 51(1):186–90.

[37] Jenkins, M. W., Chughtai, S. Q., Basavanhally, A. N., Watanabe, M., and Rollins, A. M. (2007). In vivo gated 4D imaging of the embryonic heart using optical coherence tomography. *Journal of Biomedical Optics,* 12(3):030505.

[38] Ustun, T. E., Iftimia, N. V., Ferguson, R. D., and Hammer, D. X. (2008). Real-time processing for Fourier domain optical coherence tomography using a field programmable gate array. *Review of Scientific Instruments,* 79(11):114301.

[39] Desjardins A. E., Vakoc, B. J., Suter, M. J., Sun, Y. H., Tearney, G. J., and Bouma, B. E. (2009). Real-time FPGA processing for high-speed optical frequency domain imaging. *IEEE Transactions on Medical Imaging*, 28(9):1468–72.

[40] Zhang, K., and Kang, J. U. (2010). Real-time 4D signal processing and visualization using graphics processing unit on a regular nonlinear-k Fourier-domain OCT system. *Optics Express,* 18(11):11772–84.

[41] Rasakanthan, J., Sugden, K., and Tomlins, P. H. (2011). Processing and rendering of Fourier domain optical coherence tomography images at a line rate over 524 kHz using a graphics processing unit. *Journal of Biomedical Optics,* 16(2):020505.

[42] NVIDIA, (2011). NVIDIA CUDA Compute Unified Device Architecture Programming Guide Version 4.0.

[43] Park, B. H., Pierce, M. C., Cense, B., and de Boer, J. F. (2003). Real-time multi-functional optical coherence tomography. *Optics Express,* 11(7):782–93.

[44] Wang, Y., Oh, C. M., Oliveira, M. C., Islam, M. S., Ortega, A., and Park, B. H. (2012). GPU accelerated real-time multi-functional spectral-domain optical coherence tomography system at 1300nm. *Optics Express*, 20(14):14797–14813.

[45] NVIDIA, (2011). NVIDIA CUDA CUFFT Library Version 4.0.

[46] Bonesi, M., Churmakov, D. Y., Ritchie, L. J., and Meglinski, I. V. (2007). Turbulence monitoring with Doppler optical coherence tomography. *Laser Physics Letters.* 4(4):304–07.

[47] Islam, M. S., Oliveira, M. C., Wang, Y., Henry, F. P., Randolph, M. A., Park, B. H., and de Boer, J. F. (2012). Extracting structural features of rat sciatic nerve using polarization-sensitive spectral domain optical coherence tomography. *Journal of Biomedical Optics*, 17(5):056012.

[48] Aguayo, A. J., David, S., and Bray, G. M. (1981). Influences of the glial environment on the elongation of axons after injury. *Journal of Experimental Biology*, 95(1):231–40.

[49] Shah, M. H., Kasabian, A. K., Karp, N. S., Kolker, A. R., Dublin, B. A, Zhang, L., and Sakuma, J. (1997). Axonal regeneration through an autogenous nerve bypass: an experimental study in the rat. *Annals of Plastic Surgery*, 38(4):408–14.

[50] Elbarrany, W. G., and Altaf, F. M. (2011). Ultrastructural changes in the tight intercellular junctions of the endoneurial blood vessels following sural nerve crush injury in rats. *Journal of Developmental Biology and Tissue Engineering*, 3(7):85–91.

[51] Park, B. H., Saxer, C., Srinivas, S. M., Nelson, J. S., and de Boer, J. F. (2001). In vivo burn depth determination by high-speed fiber-based polarization sensitive optical coherence tomography. *Journal of Biomedical Optics*, (6)4:474-9.

[52] Thil, M., Duy, D.T., Colin, I.M. and Delbeke, J. (2007). Time course of tissue remodeling and electrophysiology in the rat sciatic nerve after spiral cuff electrode implantation. *Journal of Neuroimmunology*, 185(1–2):103–114.

[53] Paxinos, G. (2004). *The Rat Nervous System*, 3rd ed., Elsevier, Sydney, Australia.

[54] Fontana, F., *Traitésur le Vénin de la Vipere sur les Poisons Americains*, J. Gibelin, translator, Florence, 2 volumes, pp. 187–221 (1781).

[55] Haninec, P., (1986). Undulating course of nerve fibres and bands of Fontana in peripheral nerves of the rat. *Anatomy and Embryology*, 174(3):407–11.

[56] Gratton, E., Fatini, S., Franceschini, M. A., Gratton, G., and Fabiani M. (1997). Measurements of scattering and absorption changes in muscle and brain. *Philosophical Transactions of the Royal Society of London Biological Sciences,* 352(1354):727-35.

[57] Pourmand, R., Ochs, S., and Jersild Jr., R. A. (1994). The relation of the beading of myelinated nerve fibers to the bands of Fontana. *Neuroscience,* 61(2):373–80.

[58] Clarke, E. S., and Bearn, J. B. (1972). The spiral nerve bands of Fontana. *Brain,* 95(1):1–20.

[59] Wang, Y., Henry, F., Randolph, M., de Boer, J. F., and Park, B. H. (in preparation). In vivo optical microscopy of peripheral nerve myelination with polarization-sensitive optical coherence tomography.

[60] Rylander, C. G., Dave, D. P., Akkin, T., Milner, T. E., Diller, K. R., and Welch, A. J. (2004). Quantitative phase-contrast imaging of cells with phase-sensitive optical coherence microscopy. *Optics Letters,* 29(13):1509-11.

[61] Choma, M. A., Ellerbee, A. K., Yang, C., Creazzo, T. L., and Izatt, J. A. (2005). Spectral-domain phase microscopy. *Optics Letters,* 30(10):1162-64.

[62] Joo, C., Akkin, T., Cense, B., Park, B. H., and de Boer, J. F. (2005). Spectral-domain optical coherence phase microscopy for quantitative phase-contrast imaging. *Optics Letters,* 30(16):2131-33.

[63] Ellerbee, A. K., Creazzo, T. L., and Izatt, J. A. (2007). Investigating nanoscale cellular dynamics with cross-sectional spectral domain phase microscopy. *Optics Express,* 15(13):8115-24.

[64] Joo, C., Kim, K. H., and de Boer, J. F. (2007). Spectral-domain optical coherence phase and multiphoton microscopy. *Optics Letters,* 32(6):623-5.

[65] Joo, C., Ozkumur, E., Unlu, M. S., and de Boer, J. F. (2009). Spectral-domain optical coherence phase microscopy for high-throughput protein microarray assay. *Biosensors and Bioelectronics,* 25(2):275-81.

[66] Choma, M. A., Ellerbee, A. K., Yazdanfar, S., and Izatt, J. A. (2006). Doppler flow imaging of cytoplasmic streaming using spectral domain phase microscopy. *Journal of Biomedical Optics,* 11(2):024014.

[67] Motaghian Nezam, S. M., Joo, C., Tearney, G. J. and de Boer, J. F. (2008). Application of maximum likelihood estimator in nano-scale optical path length measurement using spectral-domain optical coherence phase microscopy. *Optics Express*, 16(22):17186-95.

[68] St. Quintin, A., Merhi, L. K., and Sarunic, M. V. (2011). Spectral domain fluorescence coherence phase microscopy. *Applied Optics*, 50(12):1798-1804.

[69] Shock, I., Barbul, A., Girshovitz, P., Nevo, U., Korenstein, R., and Shaked, N. T. (2012). Optical phase nanoscopy in red blood cells using low-coherence spectroscopy. *Journal of Biomedical Optics,* 17(10):101509.

[70] Helderman, F., Haslam, B., de Boer, J. F., and de Groot, M. (2013). Three-dimensional intracellular optical coherence phase imaging. *Optics Letters*,38(4):431-33.

[71] Mujat, M., Park, B. H., Cense, B., Chen, T. C., and de Boer, J. F. (2007). Autocalibration of spectral-domain optical coherence tomography spectrometers for *in vivo* quantitative retinal nerve fiber layer birefringence determination. *Journal of Biomedical Optics*, 12(4):041205-1-6.

[72] Wojtkowski, M., Srinivasan, V., Ko, T., Fujimoto, J. G., Kowalczyk, A., and Duker, J. (2004). Ultrahigh-resolution, high-speed, Fourier domain optical coherence tomography and methods for dispersion compensation. *Optics Express*, 12(11):2404-22.

[73] Yun, S. H., Tearney, G. J., Bouma, B. E., Park, B. H., and de Boer, J. F. (2003). High-speed spectral-domain optical coherence tomography at 1.3um wavelength. *Optics Express*, 11(26):3598-3604.